

# Revealing Potential Initial Mass Function variations with metallicity: JWST observations of young open clusters in a low-metallicity environment

CHIKAKO YASUI,<sup>1</sup> NATSUKO IZUMI,<sup>2</sup> MASAO SAITO,<sup>3,4</sup> RYAN M. LAU,<sup>5</sup> NAOTO KOBAYASHI,<sup>6,7</sup> AND MICHAEL E. RESSLER<sup>8</sup>

<sup>1</sup>*National Astronomical Observatory of Japan, 2-21-1 Osawa, Mitaka, Tokyo 181-8588, Japan*

<sup>2</sup>*Institute of Astronomy and Astrophysics, Academia Sinica, No. 1, Section 4, Roosevelt Road, Taipei 10617, Taiwan*

<sup>3</sup>*National Astronomical Observatory of Japan, National Institutes of Natural Sciences, 2-21-1 Osawa, Mitaka, Tokyo 181-8588, Japan*

<sup>4</sup>*Department of Astronomical Science, School of Physical Science, SOKENDAI (The Graduate University for Advanced Studies), 2-21-1 Osawa, Mitaka, Tokyo 181-8588, Japan*

<sup>5</sup>*NSF's National Optical-Infrared Astronomy Research Laboratory, 950 North Cherry Avenue, Tucson, AZ 85719, USA*

<sup>6</sup>*Institute of Astronomy, School of Science, University of Tokyo, 2-21-1 Osawa, Mitaka, Tokyo 181-0015, Japan*

<sup>7</sup>*Kiso Observatory, Institute of Astronomy, School of Science, University of Tokyo, 10762-30 Mitake, Kiso-machi, Kiso-gun, Nagano 397-0101, Japan*

<sup>8</sup>*Jet Propulsion Laboratory, California Institute of Technology  
4800 Oak Grove Drive, Pasadena, CA 91109, USA*

(Received January 8, 2024; Revised August 14, 2024; Accepted August 23, 2024)

## ABSTRACT

We present the substellar mass function of star-forming clusters ( $\simeq 0.1$  Myr old) in a low-metallicity environment ( $\simeq -0.7$  dex). We performed deep JWST/NIRCam and MIRI imaging of two star-forming clusters in Digel Cloud 2, a star-forming region in the Outer Galaxy ( $R_G \gtrsim 15$  kpc). The very high sensitivity and spatial resolution of JWST enable us to resolve cluster members clearly down to a mass detection limit of  $0.02 M_\odot$ , enabling the first detection of brown dwarfs in low-metallicity clusters. Fifty-two and ninety-one sources were extracted in mass- $A_V$ -limited samples in the two clusters, from which Initial mass functions (IMFs) were derived by model-fitting the F200W band luminosity function, resulting in IMF peak masses (hereafter  $M_C$ )  $\log M_C/M_\odot \simeq -1.5 \pm 0.5$  for both clusters. Although the uncertainties are rather large, the obtained  $M_C$  values are lower than those in any previous study ( $\log M_C/M_\odot \sim -0.5$ ). Comparison with the local open clusters with similar ages to the target clusters ( $\sim 10^6$ – $10^7$  yr) suggests a metallicity dependence of  $M_C$ , with lower  $M_C$  at lower metallicities, while the comparison with globular clusters, similarly low metallicities but considerably older ( $\sim 10^{10}$  yr), suggests that the target clusters have not yet experienced significant dynamical evolution and remain in their initial physical condition. The lower  $M_C$  is also consistent with the theoretical expectation of the lower Jeans mass due to the higher gas density under such low metallicity. The  $M_C$  values derived from observations in such an environment would place significant constraints on the understanding of star formation.

*Keywords:* Brown dwarfs (185); Initial mass function (796); James Webb Space Telescope (2291)  
Metallicity (1031); Open star clusters (1160); Star formation (1569)

## 1. INTRODUCTION

The concept of the Initial Mass Function (IMF) was first introduced by Salpeter (1955), who found that a power-law IMF ( $dN/d\log m \propto m^{-\Gamma}$ ) with a ‘‘Salpeter index’’ of  $\Gamma = 1.35$  fit the stellar mass distribution in the solar neighborhood, where  $m$  is the mass of a star and  $N$  is the number of stars in some logarithmic mass bins. Subsequent improvements in observational instrumentation had led to the detection of turnover in IMFs in various regions, leading

to discussion of substellar IMFs (references in [Andersen et al. 2008](#)). In particular, the turnover mass, called the characteristic mass ( $M_C$ ), and its behavior with various star-forming conditions can provide valuable insights into the physical processes that regulate star and brown dwarf formation ([Luhman et al. 2000](#)). In the solar neighborhood, it has been observationally determined to be approximately constant ( $\log M_C/M_\odot \sim -0.5 \pm 0.5$ , or  $M_C \sim 0.3 M_\odot$ ) in diverse conditions ([Elmegreen et al. 2008](#)), but no models have fully explained why it can be the same. Theoretical studies point out that only massive stars can form in the first generation of stars due to inefficient cooling in extreme conditions (e.g., quite low-metallicity environment such as  $Z \lesssim 10^{-5}$ ; [Omukai et al. 2005](#)), and more recently,  $M_C$  differences for less extreme cases of metallicities have been discussed (e.g., [Chon et al. 2021](#)). However, there is little discussion as to how low at metallicity  $M_C$  begins to change.

For low-metallicity environments, globular clusters have received the most attention so far. Globular clusters have low-metallicity of  $\sim -0.5$  to  $-2$  dex ([Paresce & De Marchi 2000](#)) and they are generally well-studied due to a long history of optical observations.  $M_C$  for the clusters has been found to be similar to other regions in the solar neighborhood ([Elmegreen et al. 2008](#)). On the other hand, it has been pointed out that low-mass stars may not be kept intact in the clusters due to the dynamical evolution in the old systems ( $\sim 10^{10}$  yr), and some suggest slightly higher  $M_C$  for globular clusters compared to other local regions ([De Marchi et al. 2010](#)). Also note that, due to the old ages, the mass range for which the IMF is derived is very narrow ( $\simeq 0.1$ – $1 M_\odot$ ). This is because high-mass and intermediate-mass stars have already completed their short lives, and low-mass stars such as brown dwarfs have completed hydrogen fusion and become cold and dark, making them difficult to detect.

The Large and Small Magellanic Clouds (LMC/SMC) were targeted for IMF studies of young clusters in low-metallicity environments. However, due to the large distance of the LMC/SMC ( $\sim 50$  kpc), even with the Hubble Space Telescope, the detection limit had only reached down to  $\sim 1 M_\odot$  and never reached the  $M_C$  (e.g., [Sirianni et al. 2000](#)). For alternative targets, we have explored the outer Galaxy, which have generally low metallicities similar to the LMC/SMC ( $[\text{O}/\text{H}] \lesssim -0.5$  dex), but have significantly smaller distances ( $D \simeq 5$ – $10$  kpc). Subaru near-infrared (NIR) imaging of the star-forming regions Digel Cloud 2 ([Yasui et al. 2006, 2008](#)), S207 ([Yasui et al. 2016b](#)), S208 ([Yasui et al. 2016a](#)), S127 ([Yasui et al. 2021](#)), and S209 ([Yasui et al. 2023](#)), all selected as the region where low metallicities have actually been determined (e.g., [Rudolph et al. 2006](#)), has detected stars with masses down to about  $0.1 M_\odot$  were detected in all regions, just covering the peak of the IMF. For these regions, we primarily estimated the age and IMF at the same time, and suggested that IMFs are not significantly different from the canonical IMF. Only for S209 was the detailed derivation of the IMF attempted, suggesting it had a lower  $M_C$  ( $< 0.1 M_\odot$ ) than those generally seen in the solar neighborhood ( $\sim 0.3 M_\odot$ ), and had a slightly flatter high-mass slope ( $\Gamma \simeq -1.0$ ), IMF slope for lower masses than the first break mass, compared to the Salpeter IMF ( $\Gamma = -1.35$ ). However, because the mass detection limit did not reach masses sufficiently lower than the  $M_C$  (it only reached up to the first break mass), the actual value could not be determined.

For the next step, we obtained NIR and mid-infrared (MIR) images using JWST NIRCам/MIRI ([Izumi et al. 2024](#)), which has the highest sensitivities in both NIR/MIR among existing telescopes. Among star-forming regions in the outer Galaxy, Digel Cloud 2 was selected as the best target for derivation of substellar IMF because the derivation of IMFs for young objects requires independent information about the age ( $\sim 0.1$  Myr), which has been well studied for this region previously ([Kobayashi et al. 2008](#)). In addition, the metallicity of this region has been determined to be sufficiently low ( $\simeq -0.7$  dex) by various methods, from the radio molecular lines of molecular clouds ([Lubowich et al. 2004; Ruffle et al. 2007](#)) and optical recombination lines of an associated early type star ([Smartt et al. 1996; Rolleston et al. 2000](#)), which is another reason for selecting this region. Even for the star-forming region located in the outermost region of the Galaxy ( $D \gtrsim 10$  kpc;  $R_G \gtrsim 15$  kpc), the very high sensitivity of JWST allows us to reach the substellar mass regime ( $\sim 0.01 M_\odot$ ).

In this paper, we derive the IMF by using NIRCам imaging data in the short wavelength channel, which is the most sensitive wavelength ranges for young stars. In future papers, we will report more details on star formation in this region and discuss in particular the evolution of protoplanetary disks. This paper is organized as follows. In Section 2, we summarize previous studies of Cloud 2, focusing on studies of star-forming activities, and describe NIR deep imaging observations of the regions and data reduction with JWST/NIRCам. Section 3 describes the NIR imaging results for the two young clusters in Cloud 2. In Section 4, we construct model F200W band luminosity functions (F200W-LFs), which are used to derive the IMF, and present the best-fit IMFs obtained for the Cloud 2 clusters. In Section 5, we discuss the uncertainties in the derived  $M_C$  for Cloud 2 clusters, compare the derived  $M_C$  with previous studies, and then discuss a possible metallicity dependence of the  $M_C$ . Finally, we conclude in Section 6.

## 2. TARGET, OBSERVATIONS AND DATA REDUCTION

### 2.1. *Digel Cloud 2 clusters*

Digel Cloud 2 (hereafter, “Cloud 2”) was originally discovered as the largest and most distant molecular cloud in the CO molecular cloud survey of the Galactic anticenter ( $l = 130\text{--}155^\circ$ ) by [Digel et al. \(1994\)](#). The cloud is located in the direction of Galactic longitude  $l = 137.75^\circ$  (Galactic latitude  $b = -1.00^\circ$ ) with the LSR (local standard of rest) velocity ( $v_{\text{LSR}} = -102.4 \text{ km s}^{-1}$ ). [Digel et al. \(1994\)](#) estimated the distance of the cloud as  $R_G = 28 \text{ kpc}$  (heliocentric distance  $D = 21 \text{ kpc}$ ). [Stil & Irwin \(2001\)](#) presented H I observations that revealed a large expanding supernova remnant (SNR) shell (the center velocity of  $v_{\text{LSR}} = -94.2 \pm 0.5 \text{ km s}^{-1}$ ), GSH 138-01-94, that is associated with the Cloud 2. From the observations, they estimated the distance as  $R_G = 23.6 \text{ kpc}$  ( $D = 16.6 \text{ kpc}$ ). However, the distance to the associated early-type star MR-1 ([Muzzio & Rydgren 1974](#);  $v_{\text{LSR}} = -102.7 \pm 12 \text{ km s}^{-1}$  by [Russeil et al. 2007](#)) is estimated to have smaller values. From high-resolution optical spectra, [Smartt et al. \(1996\)](#) estimated it as  $R_G = 15\text{--}19 \text{ kpc}$  ( $D = 8\text{--}12 \text{ kpc}$ ), while [Russeil et al. \(2007\)](#) re-estimated  $R_G = 14.3 \pm 0.5 \text{ kpc}$  ( $D = 6.78 \pm 0.59 \text{ kpc}$ ).

As for star formation activity, [de Geus et al. \(1993\)](#) found an H II region associated with Cloud 2 ( $v_{\text{LSR}} = -101 \text{ km s}^{-1}$ ) that is excited by MR-1, while [Kobayashi & Tokunaga \(2000\)](#) found associated red infrared sources using the QUIST (Quick Infrared Survey Telescope), a NIR camera and 25.4 cm Cassegrain telescope, to confirm the star-forming activity in this cloud. Using the QUick InfraRed Camera (QUIRC) at the University of Hawaii 2.2 m telescope, [Kobayashi et al. \(2008\)](#) found two young embedded star clusters located in the northern and southern dense cores of the cloud, the Cloud 2-N and -S clusters, respectively. Using multiwavelength data, they presented clear evidence of sequential star formation triggered by the SNR, GSH 138-01-94. They suggest that the compression of the molecular cloud where the Cloud 2 clusters are embedded was brought on by the H I shell expansion, which is well supported from JWST observations ([Izumi et al. 2024](#)). [Kobayashi et al. \(2008\)](#) also estimated the upper limit of the age of the cluster at 0.4 Myr from the projected angular difference of the cluster from the current SNR shell front, using the distance of  $R_G = 19 \text{ kpc}$  ( $D = 12 \text{ kpc}$ ; [Smartt et al. 1996](#)). From deeper NIR imaging using the Subaru 8.2-m telescope, [Yasui et al. \(2006, 2008, 2009\)](#) discussed properties of the Cloud 2 clusters.

Recently, the Gaia Data Release 3 (Gaia DR3; [Gaia Collaboration et al. 2023](#)) has provided measurements of the distances to distant objects. The parallax for MR-1 was obtained with relatively high accuracy, with the parallax-to-error ratio of this source being more than 10, while those for the YSOs thought to be associated with the Cloud 2 in [Kobayashi et al. \(2008\)](#) (IRS 1–7) were not obtained with such high accuracy. MR-1 was matched with the Gaia source ID 461019899768797824 ( $p = 0.0992 \pm 0.0193 \text{ mas}$ ). [Bailer-Jones et al. \(2021\)](#) estimated geometric and photogeometric distances by Bayesian approach using priors based on three-dimensional model of our Galaxy. Among two types of distances, the geometric distance,  $7.9^{+1.2}_{-1.1} \text{ kpc}$ , is adopted for this target because its parallax SNR is relatively high ( $>5$ ) and the source seems to be in a crowded region judging from DSS (Digitized Sky Survey) images. Because the Gaia astrometric distance is the most reliable at this time, this value is adopted in this paper. With this adopted distance, the Galactic radius is 14.8 kpc. We also note that the upper limit of the Cloud 2 cluster age, calculated in [Kobayashi et al. \(2008\)](#) was under the assumption of the distance of 12 kpc, and we now estimate the upper limit to be 0.1 Myr using the adopted distance here, 7.9 kpc, because the expansion radius is in proportion to  $t^{2/7}$  ([Stil & Irwin 2001](#)). Therefore, we adopt the clusters’ ages of  $\simeq 0.1 \text{ Myr}$  in this paper, even considering the uncertainties of the astrometric distance.

According to the standard metallicity curve, metallicity at the Galactic radius of Cloud 2 is estimated to be  $\sim -1$  dex (e.g., [Smartt & Rolleston 1997](#)). However, it should be noted that there is a large variation in the curve, and some regions exist in environments where the metallicity is actually not as low as predicted, even though they are located in the outer Galaxy. The metallicity of Cloud 2 is therefore independently estimated at  $-0.7$  dex by using radio molecular lines ([Lubowich et al. 2004](#); [Ruffle et al. 2007](#)); this is consistent with the metallicity of MR-1 as measured by optical high-resolution spectroscopy ( $-0.5$  to  $-0.8$  dex; [Smartt et al. 1996](#); [Rolleston et al. 2000](#)). This metallicity is comparable to that of the LMC ( $-0.5$  dex at  $D \sim 50 \text{ kpc}$ ) and SMC ( $-0.9$  dex at  $D \sim 60 \text{ kpc}$ ), but given that the distance is approximately 1/5th of those, it shows that the Cloud 2 is a good target for examining individual, very low mass stars at subsolar metallicity.

### 2.2. *JWST NIRCam/MIRI imaging*

The JWST NIRCam and MIRI observations of Cloud 2 were acquired on January 17, 2023 (UT) as part of the Cycle 1 Guaranteed Time Observation (GTO) Program (Program ID: 1237, PI: Michael Ressler) Cloud 2-N was observed

with NIRCcam in six filters from 1 to 5  $\mu\text{m}$  (F115W, F150W, F200W, F356W, F444W, and F405N) with total exposure times of 344 s each, and with MIRI in three filters from 6 to 25  $\mu\text{m}$  (F770W, F1280W, and F2100W) with total exposure times of 389 s each. Cloud 2-S was observed with NIRCcam and MIRI in the same filters as Cloud 2-N, but the total exposure time was 429 s for NIRCcam and  $\simeq 400$  s for MIRI (400 s for F770W and F1280, and 411 s for F2100W). The observations themselves are summarized in [Izumi et al. \(2024\)](#). In this paper, we primarily use the NIRCcam images in the shorter wavelength filters (F115W, F150W, and F200W) because they have the highest sensitivities that allow us to derive IMFs covering the lowest mass objects possible with our JWST observations.

The NIRCcam instrument has two modules (module A and B). For the short wavelength channel (0.6–2.3  $\mu\text{m}$ ), each module has four 2K detectors with a pixel scale of  $0.031'' \text{ pixel}^{-1}$ , while each module has one 2K detectors with a pixel scale of  $0.063'' \text{ pixel}^{-1}$  in the long wavelength channel (2.4–5.0  $\mu\text{m}$ ). The detectors in the short wavelength channel are arranged in a  $2 \times 2$  array covering an area of  $2.2' \times 2.2'$  with  $4''$ – $5''$  gaps between detectors. In these observations, only module B was used due to the limited observing periods. The MIRI instrument uses three 1K arrays, one of which is used for imaging, covering  $74'' \times 113''$  with a pixel scale of  $0.11'' \text{ pixel}^{-1}$ . The field of view for MIRI imaging was set to cover almost the same area as NIRCcam imaging for Cloud 2-N, while half the area of NIRCcam imaging was covered with MIRI imaging for Cloud 2-S (see [Izumi et al. 2024](#) for these details).

Only one field of view of module B was required to cover Cloud 2-N, while one and a half fields in the long north-south direction covered Cloud 2-S. The fields of view were set so that the entire region of the Cloud 2 clusters, identified in [Yasui et al. \(2006, 2008, 2009\)](#), would be placed in one chip (not falling into the gap). For the Cloud 2-N cluster, the center of detector B4 was set to the coordinates of  $(\alpha_{2000}, \delta_{2000}) = (02^{\text{h}}48^{\text{m}}42^{\text{s}}.0, +58^{\circ}28'55''.3)$  with position angle (PA) of telescope V3 axis of 86 deg. The Cloud 2-S cluster was covered by two mosaics: the center of detector B4 was set to the coordinates of  $(\alpha_{2000}, \delta_{2000}) = (02^{\text{h}}48^{\text{m}}27^{\text{s}}.2, +58^{\circ}23'09''.8)$  with PA = 87 deg, and that of the detector B2 was set to  $(\alpha_{2000}, \delta_{2000}) = (02^{\text{h}}48^{\text{m}}28^{\text{s}}.5, +58^{\circ}23'22''.2)$  with the same PA.

Because the stellar density of cluster regions is generally high and we prefer to use point-spread function (PSF) fitting for the photometry (Section 2.3), NIRCcam subpixel dithers were adopted to improve the spatial resolution of the final combined image mosaic of all the exposures. As a result, the combined images have FWHM =  $0''.07$  for the F200W band, corresponding to spatial resolution of 550 au at the distance of 7.9 kpc.

### 2.3. Data Reduction and Photometry

All the data in each band are reduced with the standard procedure using JWST Science Calibration pipeline version number 1.9.5. Default values were used for the pipeline parameters except for “abs\_refcat”, which sets the astrometric reference catalog in Step 3. ‘GAIADR2’ was set to query the GAIA-based Astrometric Catalog web service to generate a catalog of all astrometrically measured objects in the combined field of view of the input image set in order to improve the astrometry. We also performed a custom background subtraction step since we do not have dedicated background data and nebulosity fills many of the fields of view. We estimated the background of each frame by measuring the level in several small, visually-selected regions that are free of nebulosity and then subtracting that value from the frame before combining the mosaic images. We constructed NIR pseudocolor images of Cloud 2-N and -S by combining the NIRCcam images for the F115W (blue), F150W (green), and F200W (red) bands (Figures 1 and 2, respectively).

From the Stage 3 images, we obtained NIRCcam photometry for Cloud 2-N and Cloud 2-S by fitting the PSF using IRAF<sup>1</sup>/DAOPHOT. To derive the PSF, we selected stars that were bright but not saturated, that were not close to the edge of the frame, and that did not have any nearby stars with magnitude differences  $< 4$  mag. We performed the PSF photometry in two iterations using the ALLSTAR routine: the first used the original images, and the second used the images remaining after the sources from the first iteration had been subtracted. We obtained PSF-fit radii of 1.8, 1.9, and 2.3 pixels for the full widths at half maximum in the F115W, F150W, and F200W bands, respectively, and set the inner radii and the widths of the sky annuli to be four and three times the PSF-fit radii, respectively. Because the flux calibration and zero points were in the process of being established until recently, stars in the field that were also detected with Subaru/MOIRCS in our previous study ([Yasui et al. 2009](#)) were used as photometric standards, after converting the magnitudes in the Mauna Kea Observatory (MKO) filter system ([Simons & Tokunaga 2002; Tokunaga et al. 2002](#)) to the magnitudes in the JWST/NIRCcam system using the color transformations in Appendix A. Based on the pixel-to-pixel noise in the NIR images, the  $10\sigma$  detection limits are  $m_{\text{F115W}} = 24.6$ – $24.8$  mag,  $m_{\text{F150W}} = 24.2$ – $24.6$  mag, and  $m_{\text{F200W}} = 23.6$ – $23.8$  mag in the Vega system. The  $10\sigma$  limits vary slightly from region to region depending

<sup>1</sup> NOIRLab IRAF is distributed by the Community Science and Data Center at NSF NOIRLab, which is managed by the Association of Universities for Research in Astronomy (AURA) under a cooperative agreement with the U.S. National Science Foundation.

on the exposure time and the presence of the Cloud 2 nebula. The  $10\sigma$  limits in each region, as defined in Section 3.1, are summarized in Table 1.

### 3. RESULTS

#### 3.1. Identification of the Young Clusters

In our previous studies with ground-based data, we discussed star formation markers from NIR ( $\leq 2 \mu\text{m}$ ) data only. Here, in addition to the NIR data, we can use the longer wavelength NIRCам and MIRI data to help identify regions of star forming activity and individual protostellar sources. Figures 1 and 2 show the pseudocolor images of Cloud 2-N and -S with JWST/NIRCам in the NIR. In the MIR data, star-forming regions are more prominent than in the NIR data. Observations of a particularly dense region of the molecular cloud confirmed that there are no star clusters with  $N \geq 35$  (e.g., Lada & Lada 2003) other than the Cloud 2-N, -S clusters, at least within the field of view of the observations here. An overview of star formation in Cloud 2, covered by JWST/NIRCам and MIRI in this program, is discussed in Izumi et al. (2024). Because stars in such groups share the common heritage of being formed more or less simultaneously from the same progenitor molecular cloud, their observations are very well suited for deriving initial mass functions under certain circumstances.

Figure 3 shows NIR images of the Cloud 2 clusters obtained in the NIRCам F200W band (left and right panels for the Cloud 2-N and -S clusters, respectively). The regions where particularly high stellar densities were detected in the MIRI images (see the bottom panels of Figures 5 and 6 in Izumi et al. 2024) are indicated by ellipses and are defined as cluster regions in this paper. The ellipse for the Cloud 2-N cluster has a center coordinate  $(\alpha_{2000}, \delta_{2000}) = (02^{\text{h}}48^{\text{m}}42^{\text{s}}.1, +58^{\circ}28'59''.1)$ , a minor radius of  $r_{\alpha} = 13''$  in the direction of right ascension, a major radius of  $r_{\delta} = 16''$  in the direction of declination, while the Cloud 2-S cluster has a center coordinate  $(\alpha_{2000}, \delta_{2000}) = (02^{\text{h}}48^{\text{m}}28^{\text{s}}.6, +58^{\circ}23'31''.0)$ , a minor radius of  $r_{\alpha} = 11''$  in the direction of right ascension, a major radius of  $r_{\delta} = 13''$  in the direction of declination. Note that the definitions of the cluster regions here are almost the same as in our previous studies (Yasui et al. 2006, 2008, 2009).

Cluster regions almost always contain foreground/background stars and background galaxies. Because Cloud 2 is located in the Outer Galaxy with  $R_G \simeq 17$  kpc, the cluster regions occupy very small sizes on the sky ( $\simeq 15''$  radii) and the number of such contaminants is expected to be very limited. However, given the average distribution of stars along the line of sight to this region of the Galaxy, we do expect a few non-cluster sources to be within our defined cluster regions. Therefore, it is necessary to subtract such contaminants by taking a region on the sky that is close to, but otherwise unrelated to, Cloud 2 as a control field. There is a 1 arcmin square region to the southeast of the Cloud 2-S cluster in the NIRCам images that does not otherwise overlap the star-forming regions judging from  $^{12}\text{CO}$  distributions (see Izumi et al. 2024 and Figure 11 in Yasui et al. 2008), WISE data (Figure 2 in Izumi et al. 2017), and other multiwavelength data (Kobayashi et al. 2008), shown as a white dashed square in Figure 2. We choose this area as our control field for evaluating the contamination by non-cluster sources in later sections.

#### 3.2. Reddening properties

There exist two types of reddening for sources in star-forming clusters. The first is extinction. In particular, because the Cloud 2 clusters are located at such a large distance ( $D \simeq 10$  kpc) along the plane of the Galaxy, members are subject to be extinguished by interstellar materials that exist in the direction to the clusters. In addition, clusters are embedded in molecular clouds, which also cause significant extinction. Note that the extinction from circumstellar materials is suggested that the reddening law is approximately the same as that by interstellar materials (Bouvier et al. 2013). Another reddening type is color excesses by circumstellar material. Circumstellar material is often present around young stars, which then absorbs shorter wavelength radiation and reradiates it at longer wavelengths (e.g., Lada & Adams 1992). In this section, we determine the distribution of reddening for each of the objects in the Cloud 2 clusters and consider the distribution as the probability distributions of reddening. The two reddenings are generated stochastically based on probability distribution functions and reflect them in the pseudo-generated objects in when creating the model luminosity function in Section 4.1. For this purpose, we estimate the two reddenings for each source in Cloud 2 clusters and then derive their distribution for each cluster.

We obtain reddenings for each source in Cloud 2 clusters using a color-color diagrams based on Yasui et al. (2023). They used  $H - K$  vs.  $J - H$  diagram in NIR JHK-bands, but the  $(m_{\text{F150W}} - m_{\text{F200W}})$  vs.  $(m_{\text{F115W}} - m_{\text{F150W}})$  diagram is used instead here, where  $m_{\text{F115W}}$ ,  $m_{\text{F150W}}$ , and  $m_{\text{F200W}}$  are magnitudes in the F115W, F150W, and F200W bands, respectively, since they most closely reproduce the J, H, and K bands. The  $(m_{\text{F150W}} - m_{\text{F200W}})$  vs.  $(m_{\text{F115W}} - m_{\text{F150W}})$

color–color diagrams for the Cloud 2 clusters are shown in Figure 4. All point sources that are located in the cluster regions and are detected with more than  $10\sigma$  in all F115W, F150W, and F200W bands are shown, 106 and 135 objects in total for the Cloud 2-N and -S clusters, respectively. We estimated the extinction ( $A_V$ ) and the intrinsic (dereddened) ( $m_{F150W} - m_{F200W}$ ) color  $[(m_{F150W} - m_{F200W})_0]$  for each star by dereddening it along the reddening vector (shown with black arrows in Figure 4) to the young-star locus in the color–color diagram. Because considering realistically possible IMFs, most of cluster members are expected to be M0 type or later (M0 type stars with masses of  $\simeq 1 M_\odot$ ), i.e., after the bend of the dwarf track (e.g., Bessell & Brett 1988), we approximated the young-star locus by extending the classical T Tauri star (CTTS) locus (shown with cyan lines in Figure 4) for convenience, and we used only those stars that are above the CTTS locus. When each star is dereddened to the young-star locus on the color–color diagram, the  $A_V$  values are derived based on the distance required to achieve the obtained amount of dereddening with the reddening law while the intrinsic  $(m_{F150W} - m_{F200W})_0$  are obtained from the value of  $m_{F150W} - m_{F200W}$  on the young star locus.

Although the bandpasses of F115W, F150W, and F200W are reasonably close to the JHK-band bandpasses in the conventional filter systems (cf. generally,  $J_{\text{eff}} \simeq 1.25 \mu\text{m}$ ,  $H_{\text{eff}} \simeq 1.65 \mu\text{m}$ , and  $K_{\text{eff}} \simeq 2.2 \mu\text{m}$ ; see Stephens & Leggett 2004), all of them have shorter wavelengths than the corresponding JHK-band bandpass. The filter bandpasses of F115W and F150W are shifted to the short side by about 1/3 of the bandwidth compared to J and H bands, while that of F200W is shifted to the short side by about half of the bandwidth compared to K band. This will lead to different basic properties of the color–color diagram in the NIRCcam filter system compared to those in the NIR JHK filter systems. As for the reddening law, there is a previous study using JWST/NIRCcam, where Wang & Chen (2019) evaluated the relative extinction values ( $A_\lambda/A_V$ ) in the JWST/NIRCcam filter system, based on NIR extinction law obtained from observations of red clump stars. For the CTTS locus, we derived the most plausible position of the CTTS locus in the NIRCcam filter system, shown as cyan lines (see details in Appendix A). Supplementally, dwarf-star tracks in the NIRCcam filter system are also shown as blue curves (see detail in Appendix B).

The resulting distributions of  $A_V$  and  $(m_{F150W} - m_{F200W})_0$  for the stars in the cluster regions are shown as thick lines in Figures 5 and 6, respectively. To statistically remove the effects of sources that are located in the cluster regions but are foreground or background stars, we also derived the distributions in the control field using the color–color diagram for stars in the control field, shown in Figure 7. The obtained distributions were normalized by multiplying the ratio of the area of each cluster region to the area of the control field and are shown as thin lines in Figures 5 and 6. In Figure 5, the distribution of stars in the cluster region minus the distribution of stars in the control field is shown by the red line, which is approximately the distribution of cluster members.

In Figure 5, the  $A_V$  distribution of stars in the control field decreases monotonically with increasing  $A_V$ , reaching almost zero at  $A_V = 5$  mag. In the cluster regions, on the other hand, the distribution extends to larger values of  $A_V \simeq 15$  mag for both clusters. The reason why stars in the cluster region have such large  $A_V$  values may be that they are subject to large extinction by the interstellar medium due to the relatively large distance to Cloud 2. In addition, the large dispersion of  $A_V$  values should be due to the fact that star-forming molecular clouds are still present in this star-forming region. Because Kobayashi & Tokunaga (2000) confirmed that no foreground clouds exist in the direction of Cloud 2 from the  $^{12}\text{CO}$  survey data of the Five College Radio Observatory (FCRAO) (Heyer et al. 1998), those in the  $A_V$  range whose counts in the cluster region are significantly larger than those in the control field and those with large  $A_V$  values can be considered cluster members.

The sources with  $A_V \gtrsim 5$  mag clearly appear to be cluster members, but there also appear to be sources with relatively small  $A_V$  of 1–2 mag for both Cloud 2-N and -S clusters. However, when figures are produced in a different bin from Figure 5 (e.g.,  $\Delta A_V = 1.5$  mag), the peak is no longer seen in the distribution for Cloud 2-N, while the peak is still seen for Cloud 2-S. This suggests that there are indeed cluster members with relatively small values for Cloud 2-S only. Therefore, most of stars in the range of  $A_V \geq 2$  mag and  $A_V \geq 1$  mag for Cloud 2-N and -S clusters, respectively, where the number of objects in the cluster region is much larger than the number of objects in the control region continuously, are considered to be from Cloud 2 clusters.

It should be noted that all sources in the control field have extinctions significantly lower than the median for objects in the cluster area. This may indicate that the background contamination is negligible, but in fact it may simply indicate that while background stars are present, the extinction due to molecular clouds is much lower in the control field. In the latter case, it would be incorrect to remove the influence of background sources here. To verify this, we set a region north of the Cloud 2-S cluster region, shown as the region enclosed by a dotted square in Figure 2, as another control field and obtained the  $A_V$  distribution in the same way as for the original control field. In Izumi et

al. (2024), the region was confirmed to have no significant star forming activities and a CO molecular cloud column density similar to the Cloud 2-N and -S cluster regions. The derived  $A_V$  distribution is quite consistent with the original control field distribution. Therefore, we can conclude that the influence of background stars in these regions is negligible.

In Figure 6, the  $(m_{F150W} - m_{F200W})_0$  distribution of stars in the control field increases from  $(m_{F150W} - m_{F200W})_0 = 0$  mag to 0.4–0.5 mag and then decreases (to zero at about 0.6 mag), while the distributions of stars in the Cloud 2-N and -S cluster regions increase from  $(m_{F150W} - m_{F200W})_0 = 0$  mag to 0.5–0.6 mag and extend up to  $(m_{F150W} - m_{F200W})_0 \simeq 1.0$  mag. The larger  $(m_{F150W} - m_{F200W})_0$  of the stars in the cluster region is due to the color excess produced by the circumstellar material around the young stars. We assume that this excess is only a F200W-band excess (Strom et al. 1989; abbreviated “F200W-excess”). We take the average value of the  $(m_{F150W} - m_{F200W})_0$  of stars in the control field, which is estimated to be 0.45 mag, as a typical  $(m_{F150W} - m_{F200W})_0$  value of stars without any surrounding materials,  $(m_{F150W} - m_{F200W})_{0,\text{crit}} = 0.45$  mag.

We consider stars with  $(m_{F150W} - m_{F200W})_0 \geq (m_{F150W} - m_{F200W})_{0,\text{crit}}$  to be stars with a F200W-excess, which we define as  $(m_{F150W} - m_{F200W})_0$  minus  $(m_{F150W} - m_{F200W})_{0,\text{crit}}$ , while stars with  $(m_{F150W} - m_{F200W})_0 \leq (m_{F150W} - m_{F200W})_{0,\text{crit}}$  are considered to be stars without a F200W-excess. The resulting distributions of F200W-excess are shown in Figure 8. The distributions for stars in the Cloud 2-N and -S cluster regions are shown in the left and right panels, respectively. As in Figures 5 and 6, distributions for stars in the cluster regions are shown with thick lines, while those for stars in the control field are shown with thin lines. The subtracted distributions are shown with red lines. In a later section, we use the subtracted distributions of stars for the Cloud 2-N and -S clusters to construct model F200W-LFs for evaluating the IMF.

### 3.3. Mass- $A_V$ limited samples

We extract mass- $A_V$ -limited samples from the color–magnitude diagram for each cluster in the same way as Yasui et al. (2023). We constructed the  $m_{F150W} - m_{F200W}$  versus  $m_{F200W}$  color–magnitude diagrams for the point sources detected in the Cloud 2 cluster regions in Figure 9 (left and right panels for the Cloud 2-N and -S clusters, respectively). All point sources that are detected with more than  $10\sigma$  in both the F150W and F200W bands are shown. The dashed lines mark the  $10\sigma$  limits. The gray lines in these figures show isochrone tracks for the age of 0.1 Myr: from Siess et al. (2000) for the mass range  $3 < M/M_\odot \leq 7$ ; and from D’Antona & Mazzitelli (1997, 1998) for the mass range  $0.017 \leq M/M_\odot \leq 3$ . Model selection is discussed in Section 4.1. The tickmarks on the isochrone models, which are shown in the same colors as the isochrone tracks, correspond to the positions of stellar masses 0.02, 0.03, 0.04, 0.06, 0.08, 0.1, 0.5, 1, 3, and  $5 M_\odot$ . The arrows indicate the reddening vector for  $A_V = 5$  mag.

We define the mass- $A_V$ -limited sample for the assumed distance and age. We refer to Figure 5 to limit the extinction range. As discussed in Section 3.2, we set the minimum values of  $A_V$  to be 2 mag and 1 mag for the Cloud 2-N and -S clusters, respectively. On the larger  $A_V$  side, more stars can be extracted in the cluster field with a larger  $A_V$  threshold, but if the  $A_V$  range is set to a very large value, the mass detection limit becomes large when defining the Mass- $A_V$ -limited sample. Because in the cluster region the  $A_V$  distributions for both clusters break off around  $A_V \simeq 15$  mag, we set the upper limit of the  $A_V$  range here as  $A_V = 14$  and  $A_V = 18$  mag for the Cloud 2-N and 2-S clusters, respectively. In this case, the mass-sensitivity limits in the defined  $A_V$  range are indicated by red lines, and the mass detection limits correspond to  $\simeq 0.02 M_\odot$  for both clusters.

In Figure 9, our mass- $A_V$ -limited samples are shown in red and outliers are shown in black. We note that the samples obtained here may still contain some foreground (and sometimes background) sources; the color–magnitude diagram of the control field is shown in Figure 10 and shows that a few sources still meet our selection criteria. In the control field, the most of objects are located around  $(m_{F150W} - m_{F200W}) \simeq 0.5$  mag, whereas most sources in the clusters have  $(m_{F150W} - m_{F200W}) > 0.5$  mag, with the center of distribution at  $(m_{F150W} - m_{F200W}) \sim 1.0$  mag. This is because the sources in the cluster are subject to local extinction, considering the Cloud 2 clusters are embedded clusters. Because of this feature, the number of stars in the control field selected by the sample selection method is very small, especially at  $m_{F200W} \gtrsim 18$  mag, where the PMS track is particularly red. This suggests that the Mass- $A_V$ -limited sample of clusters contains very few foreground sources. In fact, the effect of foreground stars on the F200W-LFs constructed in Section 3.4 to derive the IMF is confirmed to be negligible.

However, in order to assess and minimize the influence of foreground stars, we obtain the pseudo-mass- $A_V$ -limited samples in the control field in the same way as in the cluster region (Figure 10), and subtract the number of pseudo-sources obtained in the control field from the number of sources in each cluster region when constructing the F200W-

LFs for the IMF derivation in the next section (Section 3.4). In that section, the number of pseudo-mass- $A_V$ -limited samples in the control field is normalized by multiplying the ratio of the area of each cluster region to the area of the control field. The final number of objects in the Cloud 2-N and -S clusters are estimated to be 52 and 91, respectively.

### 3.4. Cluster F200W-LFs

We constructed the F200W-LF for each cluster using the mass- $A_V$ -limited samples extracted in Section 3.3. (left and right panels in Figure 11 for Clouds 2-N and -S clusters, respectively). In this figure, the F200W-LFs for sources in the cluster regions (the cluster region F200W-LFs) are shown with thick black lines, while those for sources in the control field (the control field F200W-LF) are shown with thin lines. The control field F200W-LF is normalized by multiplying the ratio of the area of each cluster region to the area of the control field. We subtracted the normalized counts from the control field F200W-LF from the counts for each cluster region F200W-LF to obtain the cluster F200W-LFs, which are shown as thick red lines. The F200W-LFs for the Cloud 2 clusters monotonically increase up to  $m_{\text{F200W}} \sim 20$  mag for both clusters, and then decrease as  $m_{\text{F200W}}$  magnitudes become even fainter. In general, the F200W-LF peak reflects the IMF peak. However, the counts may just appear to decrease after  $m_{\text{F200W}} \sim 20$  mag because we are taking mass- $A_V$ -limited samples here, rather than showing IMF turnover. In fact, the color-magnitude diagrams (Figure 9) show that for  $m_{\text{F200W}} \lesssim 21$  mag there are stars in all  $A_V$  ranges, sandwiched by two orange lines (isochrone tracks with minimum and maximum  $A_V$  values, i.e., all  $A_V$  ranges), whereas for  $m_{\text{F200W}} \gtrsim 21$  mag there are stars only in the larger  $A_V$  ranges, sandwiched with red line (showing the sensitivity limit) and an orange line (showing isochrone track with maximum  $A_V$  value). Also, note that the counts of the control field are very small ( $N \lesssim 5$ ) in both clusters. In particular, there are almost no counts of the control field around the F200W-LF peak, suggesting that the influence of the foreground is negligible.

Also, it should be noted that the detection completeness of stars with  $>10\sigma$  detection is generally almost one, whereas that of the fainter stars is less than one (e.g., Minowa et al. 2005). Actually, Yasui et al. (2008) confirmed the same results from estimation of the detection completeness for the Subaru/MOIRCS ground-based data by putting artificial stars at random positions in the Cloud 2 cluster regions and checking whether they are detected in the same way as the real objects. Because data from JWST has much high qualities, e.g., high spatial resolutions and low background noise, this should hold (or the situation should be even better) for the JWST data here and the brightness completeness may be at fainter magnitudes. Considering the  $10\sigma$  detection magnitude shown in Table 1, the completeness should be  $\sim 1$  in the all magnitude bins of the Cloud 2 clusters' F200W-LFs.

In later sections, the cluster F200W-LFs obtained here will be compared to the model F200W-LFs that are constructed considering the same mass- $A_V$ -limited sample as for the observations, to derive the IMF. A similar method was used in the Trapezium cluster of Muench et al. (2002), but it was necessary to consider background sources as contamination in addition to foreground sources for nearby clusters such as the Trapezium cluster, thus accounting for complex reddening. On the other hand, in the case of Cloud 2 clusters, the effect of foreground stars on the F200W-LF is confirmed to be almost nonexistent, and there are no objects with large  $A_V$  in the control field, suggesting that the effect of background stars is also almost nonexistent. This is a similar trend for other star-forming clusters located in the outer Galaxy compared to previous studies (Yasui et al. 2016a, 2021, 2023).

## 4. DERIVATION OF THE CLOUD 2 CLUSTERS' IMF

### 4.1. Modeling

We derive the IMF for Cloud 2 clusters in the Outer Galaxy, which as we have previously noted is in a low metallicity environment. The most basic way to derive IMFs is to derive masses for individual stars, and this method has often been used to derive IMFs for nearby star forming regions (e.g. Hillenbrand 1997; Luhman et al. 2000). The most precise way to derive masses (and ages) for individual stars to derive IMFs is using HR diagrams from spectroscopic observations. However, it takes a great deal of time to obtain sufficiently sensitive spectra to be used for the classification when targeting these very distant regions. Conversely, here we derive the IMF from imaging data only, using a method that was originally developed by Muench et al. (2002) to derive the IMF for the Trapezium cluster in Orion and then modified by Yasui et al. (2023). Note that the IMF obtained with this method for the Trapezium cluster was consistent with the IMF obtained with the derived masses for individual stars using spectroscopic data, but the method could derive IMFs for much lower mass stars, compared to the IMFs obtained from spectroscopic data (see Muench et al. 2002).



In our modeling, we first generated stars with masses determined probabilistically according to IMFs. We assume a log-normal IMF (Miller & Scalo 1979),  $dN/d\log m \propto \exp(-C \times (\log m - \log M_C))$ , and a tapered power-law (TPL) IMF<sup>2</sup> (De Marchi et al. 2010),  $dN/d\log m \propto m^{-\Gamma} \{1 - \exp[-(m/M_C)^\beta]\}$ . The counts of F200W-LF first increase for fainter magnitudes ( $m_{\text{F200W}} \lesssim 18$  mag), then become almost flat ( $m_{\text{F200W}} \simeq 18$ –20 mag), before decreasing ( $m_{\text{F200W}} \gtrsim 21$  mag), but it is not obvious at this stage whether the trend in F200W-LFs counts reflects a similar trend in IMFs (Section 3.4). Even these cases can be expressed by log-normal or TPL IMF: in the case of monotonic increase, the peak mass should be estimated to be smaller than the minimum mass range, and in the case of flattening after monotonic increase, the peak mass should be estimated to be slightly larger than the minimum mass range. The ranges of parameters for both IMF indices are set within relatively realistic ranges of values:  $C = 0.1$  to 10 and  $\log M_C = -2.0$  to 0.0 for log-normal IMF, and  $\Gamma = 0.5$  to 2.0,  $\log M_C = -2.0$  to 0.0, and  $\beta = 0.5$  to 4.0 for TPL IMF. All parameter combinations are tried in the set parameter range, in increments of 0.1 for all parameters. The IMF mass range is set to cover all possible ranges obtained from mass- $A_V$ -limited samples the magnitude range of F200W LF used for model fitting discussed in Section 4.2.

We then determined NIR luminosities for the artificially generated sources based on the IMFs. We used the mass–luminosity (M–L) relations employed in Section 3.3 for the isochrone tracks in the color–magnitude diagram. The M–L relation assuming the most reliable distance (7.9 kpc) and age (0.1 Myr) is shown as a black line in Figure 12. Regarding the choice of the isochrone model, Muench et al. (2000, 2002) found that variations in the pre-main-sequence (PMS) M–L relation, which result from differences in the adopted PMS tracks, produce only small effects in the form of the model luminosity functions, and these effects are mostly likely not detectable observationally. Lada & Lada (2003) also pointed out that the predicted luminosities are essentially degenerate with respect to different models (see their Figure 7), and they suggested that this should be due to the fact that the luminosity of a PMS star is determined by very basic physics, simply the conversion of gravitational potential energy to radiant luminosity during Kelvin-Helmholtz contraction.

Yasui et al. (2023) compared low-metallicity models (down to  $[M/H] = -2.0$ ) with solar metallicity models and found that the differences in the M–L relation due to changes in metallicity within the same group of models were very small. They also confirmed that the differences in metallicity were significantly smaller than the differences between models by different groups. Therefore, the model with solar metallicity ( $[M/H] = 0.0$ ) was adopted here. We also adopt the K-band luminosity for use as the F200W-band luminosity. The difference between these luminosities is discussed in Section 5.1. The isochrone model for the age of the Cloud 2 clusters, 0.1 Myr, was used, and age spread was not taken into account here because Muench et al. (2000) found that variations in the cluster-age spread have only a small effect on the form of the KLF and would also be difficult to distinguish observationally.

The effects of M–L relations by the difference of filter system will be discussed in Section 5.1. After conversion of mass to luminosity, luminosity was converted to NIR magnitudes considering the distance, then the effects of reddening are also considered. The reddening (extinction and infrared disk excess) was generated stochastically using the reddening probability distribution for the Cloud 2 clusters obtained in Section 3.2.

Obtained magnitudes and colors for pseudo-generated sources are confirmed whether they satisfy the criteria for mass- $A_V$ -limited sample in Section 3.3, and if they do not meet the criteria, they are not counted in the model F200W-LF. This process was repeated until the number of stars satisfying this condition became equal to the number of stars in the mass- $A_V$ -limited samples for the Cloud 2 clusters that we had obtained by subtracting the number of samples in the control field from the number of samples in the cluster region. For each synthetic cluster, the obtained magnitudes were binned by one magnitude and compared to the F200W-LFs of the observed clusters to derive the best IMF. For both Cloud 2-N and -S, 100 independent F200W-LFs were generated for each IMF. The average and corresponding  $1\sigma$  standard deviation of these 100 F200W-LFs were calculated.

#### 4.2. The IMFs Derived for the Cloud 2 clusters

For deriving best-fit IMF for the Cloud 2 clusters, chi-square test are carried out. It should be noted that there must be sufficiently large numbers of frequencies in the bins for this test. According to a textbook (Wall & Jenkins 2012), the expected frequencies should be  $>5$  in  $>80\%$  of the bins, in particular because of the severe instability at  $<5$  counts per bin. To meet this requirement, four bins of  $m_{\text{F200W}} = 18$ –22 mag for Cloud 2-N and five bins of  $m_{\text{F200W}} = 17$ –22

<sup>2</sup> De Marchi et al. (2010) defined the TPL IMF as  $dN/dm \propto m^{-\alpha} [1 - \exp(-m/M_C)]$ , where  $\alpha$  is the index of the power law in the upper end of the mass function and  $\beta$  is the tapering exponent to describe the lower end of the IMF. This formula can be rewritten as  $dN/d\log m \propto m^{-\Gamma} \{1 - \exp[-(m/M_C)^{\gamma+\Gamma}]\}$ , where  $\Gamma$  is the slope in the high-mass regime and  $\gamma$  is the slope in the low-mass regime, and  $\gamma + \Gamma$  is denoted here as  $\beta$ .

mag for Cloud 2-S can be used for the fit. Because the log-normal and TPL IMFs have two and three parameters, respectively, only log-normal IMF can be used for the Cloud 2-N while both log-normal and TPL IMFs can be used for the Cloud 2-S. As a result of F200W-LF fitting, we obtained reduced  $\chi^2$  values of  $\simeq 1$  from the best-fit IMF parameter sets for both clusters. The obtained best-fit IMF parameters for the Cloud 2-N and -S clusters are shown in Tables 2 and 3 for log-normal and TPL IMFs, respectively, with the ranges corresponding to the 68% confidence levels shown in brackets. The model F200W-LFs for the Cloud 2-N and -S clusters using the parameters for the best-fit log-normal IMFs are shown in Figure 13, along with observed F200W-LFs (left and right panels for Cloud 2-N and -S clusters, respectively). The red lines show best-fit model F200W-LFs with  $1\sigma$  standard deviation, while blue histograms show observed cluster F200W-LFs. The bins of the fit range are indicated by filled blue squares, and the others by open blue squares. The best-fit IMFs for the Cloud 2-N and -S clusters are also shown in Figures 14 and 15, respectively, shown as black lines. For reference, IMFs obtained in previous studies in the solar neighborhood are also shown as colored lines: Salpeter (1955, magenta), Scalo (1998, green), Muench et al. (2002, red), Miller & Scalo (1979, blue), and Kroupa (2002, orange). All of the IMFs are normalized to 0 on the vertical axis at a mass of  $1 M_\odot$ .

The  $M_C$  values are estimated as  $\log M_C = -1.5_{-0.2}^{+0.1}$  for the Cloud 2-N cluster based on log-normal IMF, and  $\log M_C = -1.6_{-0.4}^{+0.2}$  and  $-1.4_{-0.3}^{+0.4}$  for the Cloud 2-S clusters based on log-normal IMF and TPL IMF, respectively. Because the mass detection limits are  $0.02 M_\odot$  ( $-1.70$  on the log scale) for both Cloud 2 clusters, which are lower than the  $M_C$  value obtained here, our observations are considered to cover the IMF peaks for both clusters and the  $M_C$  values obtained here are considered to be significant. This is the first derivations of  $M_C$  for star-forming clusters in a low-metallicity environment, which was achieved due to the quite high sensitivities of the JWST. We note that the  $M_C$  values for both clusters are very similar although there is some scatter in each value.

In the fitting results assuming log-normal IMF for the Cloud 2-S cluster, the high-mass slope appears unrealistically steep although they cannot be rejected from the chi-square test. This may be because the log-normal function defines the IMF symmetrically, and the slope on the high-mass side and the low-mass side are only defined at the same value. Therefore, the fit may not work very well for the Cloud 2-S cluster, where the fit was performed over a relatively wide range of grades (i.e., corresponding to a wide mass range). The TPL IMF seems to improve on this point although the uncertainties here is very large. In any case, the derivation of  $M_C$ , the most noteworthy point of this paper, yielded similar values for both assumed IMFs within the error range.

Here the F200W-LF bins are taken as  $m_{\text{F200W}} = 15.0\text{--}16.0, 16.0\text{--}17.0, \dots, \text{and } 21.0\text{--}22.0$  mag. The fits of LFs with the center of the bin shifted by 0.5 mag ( $m_{\text{F200W}} = 15.5\text{--}16.5, 16.5\text{--}17.5, \dots$ ) are also attempted. As a result, the obtained best-fit IMF parameters assuming log-normal IMF for the Cloud 2-N are  $\log M_C = -1.5_{-0.5}^{+0.3}$  ( $C = 0.9_{-0.8}^{+2.9}$ ), while the parameters assuming log-normal and TPL IMFs for the Cloud 2-S cluster are  $\log M_C = -1.7_{-0.3}^{+0.2}$  ( $C = 2.2_{-0.9}^{+1.2}$ ) and  $\log M_C = -1.7_{-0.3}^{+1.5}$  ( $\Gamma = 0.9_{-0.2}^{+1.1}$  and  $\beta = 0.9_{-0.3}^{+2.4}$ ), respectively. The obtained  $M_C$  values are not significantly different from those obtained with the original LF bin settings.

We also note that there are large uncertainties in the derived IMF parameters, especially for parameters related to high-mass slope,  $C$  for log-normal IMF and  $\Gamma$  for TPL IMF. The main reason for this should be simply the small number of members in the two clusters (52 and 91 for the Cloud 2-N and -S clusters, respectively), as discussed in Yasui et al. (2023). In particular, the  $\Gamma$  in the TPL IMF fit for the Cloud 2-S cluster shows that the 68 % confidence level is satisfied for almost all the originally input parameter ranges, suggesting that the uncertainties of  $M_C$  be even larger. However, since fitting with parameters that are far from reality is probably meaningless, further fitting with a wider range of parameters is not performed here.

## 5. DISCUSSION

### 5.1. Uncertainties in the derived $M_C$ for Cloud 2 clusters

Very similar values of  $M_C$  are obtained for Cloud 2-N and -S clusters, and although the  $M_C$  values have large uncertainties, this suggests that the value is typical for the region,  $\log M_C \simeq -1.5$ . We discuss possible uncertainties of  $M_C$  besides the uncertainties obtained from the F200W-LF fitting in Section 4.2. First, as for the distance of the Cloud 2 clusters, the astrometric distance  $D = 7.9$  kpc from Gaia DR3 was adopted in this paper (Section 2.1). The distance has uncertainties of  $\simeq 1$  kpc, which cause a difference of distance modulus  $\Delta m = 0.3$  mag. The  $M_C$  obtained from the F200W-LF fit assuming the most reliable age (0.1 Myr),  $\log M_C \simeq -1.5$  or  $M_C = 0.03 M_\odot$ , corresponds to  $m_{\text{F200W}} = 21.4$  mag under  $A_V = 5$  mag. In the case of smaller (larger) distances by 1 kpc, the magnitude corresponds to a decrease (an increase) in mass of  $0.01 M_\odot$  (see the black line in Figure 12).

It is possible that some objects in this study cannot be resolved at the spatial resolution of  $\lesssim 500$  au (Section 2.1); this will influence the derived  $M_C$  value. The binary fraction is known to be smaller for lower-mass stars (Offner et al. 2023). In the mass range around  $M_C$ , the fraction is  $\simeq 20\%$  at  $0.1 M_\odot$  and  $\simeq 10\%$  at  $0.05 M_\odot$ . For FGK-type dwarfs, the fraction of close binaries ( $< 10$  au) is known to increase strongly with decreasing metallicity, while the fraction of wide binaries ( $\gtrsim 200$  au) is known to be relatively constant over  $-1.5 \lesssim [\text{Fe}/\text{H}] \leq 0.5$  (Moe et al. 2019). If this is also the case for the low mass stars such as those targeted here, then there may be more binaries in Cloud 2, which is in a low-metallicity environment. The binary fractions for open clusters are known to be consistent with the fractions listed above, which are mainly derived from field stars, for close and intermediate binaries, while those for wide binaries are smaller than the field values. The discrepancies in the wide binary fraction exist between the dense Orion Nebula Cluster and the sparse Taurus star-forming region, which exhibit a deficit and excess, respectively, compared to the field main sequence stars (Duchêne et al. 2018; Kraus et al. 2011). The two clusters in Cloud 2 have different stellar densities (see Figure 8 in Yasui et al. 2008): the Cloud 2-N cluster is a Taurus-like sparse cluster ( $\simeq 20$  stars  $\text{pc}^{-2}$ ), while the Cloud 2-S cluster is Orion Nebula Cluster (ONC)-like dense cluster ( $\simeq 70$  stars  $\text{pc}^{-2}$ ). Despite these differences, the derived  $M_C$  values for the clusters are nearly identical, implying that this effect is very small, if it exists at all. Taking into account the unresolved binaries, the stellar mass and thus the  $M_C$  is estimated to be larger than it actually is. We assume the extreme case where all objects are unresolved binaries and the binaries have the same mass. The flux corresponding to  $M_C$  ( $m_{\text{F200W}} = 21.4$  mag) would consist of two objects with  $m_{\text{F200W}} = 22.2$  mag, corresponding to a mass reduction of  $0.01 M_\odot$  (see the black line in Figure 12).

In Chabrier (2003), it was argued that the discrepancy between the  $M_C$  of the IMF for the unresolved system IMF ( $\sim 0.2 M_\odot$ ) and that for the single-star IMF ( $\sim 0.08 M_\odot$ ) is explained by considering unresolved stars. Since also for the target clusters here the sources cannot be resolved within  $\lesssim 500$  au, the obtained  $M_C$  should be the upper limit of the single-star IMF, and the single-star IMF is expected to have an even smaller value than the  $M_C$  here. As mentioned above, it is suggested that the overall binary fraction tends to increase with decreasing metallicity, and taking this effect into account, the single-star IMF may take a value even smaller than that expected from the ratio of the system IMF to the single-star IMF in the solar neighborhood.

In the F200W-LF fitting, we used K-band luminosities from the M–L relation by D’Antona & Mazzitelli (1997, 1998) for low-mass stars,  $0.017 \leq M/M_\odot \leq 3$ . Although the effects of adopting different models are thought to be mostly likely not detectable observationally as discussed in Section 4.1, we checked the effects of differences in filter systems (F200W vs. K) adopted in the models. The model by D’Antona & Mazzitelli (1997, 1998) consider canonical NIR filter system, while the model by Baraffe et al. (2015) provides optical/NIR/MIR magnitudes in a variety of filter systems, including JWST/NIRCam filter system. The model by Baraffe et al. (2015) covers mass range of  $0.01\text{--}1.4 M_\odot$ . Because only models for ages of  $\geq 0.5$  Myr (older than clusters’ ages) are available, we could not use it for the F200W-LF fitting in Section 4.1, but here we compare the two models for an age 0.5 Myr. In Figure 12, the M–L relation by Baraffe et al. (2015) for the age of 0.5 Myr in the JWST/NIRCam is shown with a blue line, while that used in the modeling in Section 4.1 (Siess et al. 2000; D’Antona & Mazzitelli 1997, 1998) for the same age is shown with a gray line. In the mass range where both models exist, the difference in magnitudes between the two models at the same mass is 0.2 mag on average (0.4 mag at most), which is significantly smaller than the F200W-LF bin of 1 mag. In the magnitude corresponding to the mass of  $M_C$  ( $m_{\text{F200W}} = 21.4$  mag), the mass estimated from Baraffe et al. (2015) is almost identical to that from D’Antona & Mazzitelli (1997, 1998).

The final concern is the uncertainty in the cluster ages. Although the discussion proceeded by assuming the most plausible age of the clusters,  $\simeq 0.1$  Myr (Section 2.1), the F200W-LF fitting for older ages are also attempted. It is known that the embedded phases of clusters last about 2–3 Myr (Lada & Lada 2003), and indeed clusters are known to be sufficiently embedded in molecular clouds (Izumi et al. 2024) to suggest that the age of clusters should not exceed 2 Myr at most. We performed F200W-LF fitting for ages up to 2 Myr (0.5, 1, and 2 Myr) as well for the both Cloud 2 clusters, using the M–L relations in the JWST filter system discussed above. The  $M_C$  is estimated as  $\log M_C = -0.9$  to  $-1.0$  for all assumed ages for both Cloud 2 clusters. The estimated value is also approximately consistent with the value read from Figure 12, which in turn supports the fits here work well.

In summary, it is suggested that the  $M_C$  can range from  $0.02\text{--}0.1 M_\odot$  ( $\log M_C \simeq -1.7$  to  $-0.9$ ) although the  $M_C$  obtained here have various kind of uncertainties. In the next section, we discuss the possible metallicity dependence of  $M_C$  by comparison with  $M_C$  for other derived regions in previous studies. While it should be noted that the uncertainty of the  $M_C$  in Cloud 2 is somewhat large, the  $M_C$  here is found to be smaller compared to previous derivations.

### 5.2. Possible metallicity dependence of $M_C$

Because star-forming open clusters generally have similar characteristics, e.g., young age ( $\sim 10^6$ – $10^7$  yr) and moderate cluster scale ( $N_* \lesssim 10^3$ ) (Portegies Zwart et al. 2010), they are a good basis for comparison to evaluate the metallicity dependence of  $M_C$ . Previous studies compiled  $M_C$  for local open clusters, and found  $M_C$  in all regions is about constant,  $\log M_C/M_\odot \sim 0.5 \pm 0.5$ , or  $M_C \sim 0.3 M_\odot$  (e.g., Elmegreen et al. 2008). Elmegreen et al. (2008) suggested that the thermal Jeans mass ( $M_J$ ), which is expected to be proportional to  $M_C$ , depends weakly on environment, such as density, temperature, metallicity, and radiation field. The  $M_C$  values for the Cloud 2 clusters we have derived here ( $M_C \simeq -1.5$ ) are lower than the  $M_C$  values estimated for local open clusters although with larger uncertainties ( $\simeq 0.5$  in log scale). The lower  $M_C$  values of the Cloud 2 clusters suggest that  $M_C$  is correlated with metallicity.

Because globular clusters have low metallicities ( $[\text{Fe}/\text{H}] \simeq -0.70$  to  $-2.2$ ) similar to Cloud 2, but have much older ages ( $\sim 10^{10}$  yr old), they are also good comparisons for understanding the evolution of the IMF. Elmegreen et al. (2008) and Paresce & De Marchi (2000) claim that the  $M_C$  of the globular clusters is approximately similar to other local regions, while De Marchi et al. (2010) claimed that  $M_C$  for globular clusters are higher ( $M_C \simeq 0.33 M_\odot$ ) than young open clusters ( $M_C \simeq 0.15 M_\odot$ ). Despite the fact that the Cloud 2 clusters have a similarly low metallicity (although on the higher end of metallicity among globular clusters), the obtained  $M_C$  values for the Cloud 2 clusters are lower than those for the globular clusters. The main reason for this could be due to the loss of low-mass stars in globular clusters through dynamical evolution, as pointed out in De Marchi et al. (2010). In other words, the Cloud 2 clusters targeted here are so young that they have not yet experienced dynamic evolution and they are likely to keep literally their *initial* MF. Actually, no brown dwarfs have been identified in any globular clusters to date although some candidates have been found recently (e.g., Dieball et al. 2019, Nardiello et al. 2023). This is because, in addition to their possible loss from globular clusters due to dynamical evolution, brown dwarfs cannot sustain hydrogen fusion and they become cooler and fainter with time. Therefore, our detection of such low-mass sources in clusters with low metallicity is also one of the significant results of our observations here.

The ages of the Cloud 2 clusters are estimated to be very young, and there are very few examples of such young star-forming regions in the solar neighborhood. Nevertheless, at least for the currently detected sources, the color-color diagrams (Figure 4) show that the color excesses from circumstellar materials are very small (see also Yasui et al. 2009), and there are few sources detected at wavelengths longer than  $2 \mu\text{m}$ , but not here down to  $2 \mu\text{m}$  (see Izumi et al. 2024). Therefore, because it is unlikely that the masses of some of the currently detected or undetected sources will become significantly larger in the future, the initial mass function will change drastically in the future for sources produced in the same generation.

For local field stars, there are recent updates with highly accurate IMFs derived from Gaia data. Hallakoun & Maoz (2021) derived the IMF of stars within 250 pc and in the mass range of  $0.2$ – $1.0 M_\odot$  using Gaia DR2. They derived the IMF by classifying stars into four categories: thin-disc population, thick-disc stars, high-metallicity halo, and low-metallicity halo ( $[\text{M}/\text{H}] < -0.6$ ). For the first three populations, IMFs are found to be similar to other local regions, with  $\log M_C \sim 0.5 M_\odot$ , while only low-metallicity halo stars show a bottom-heavy IMF and are well described by a single power law over most of the mass range, indicating that  $M_C$  is lower than  $0.2 M_\odot$ . The results seem consistent with our results here, in that  $M_C$  is found to be smaller than  $0.2 M_\odot$ , although it should be noted that the low-metallicity halo is likely to be the debris from events, e.g., accretion by the Milky Way, that occurred very long ago ( $\sim 10$  Gyr ago). However, Li et al. (2023) derived the IMF based on  $\sim 93,000$  spectroscopically observed M dwarfs (the mass range of  $0.3$ – $0.7 M_\odot$ ) located within  $100$ – $300$  pc, in combination with Gaia DR3, and discussed the variation of the IMF with metallicity and time. They suggested that the stellar population that formed at the earliest times contains fewer low-mass stars compared to the canonical IMF, independent of stellar metallicity, while the fraction of low-mass stars increases with stellar metallicity in present days. Their suggestion seems to be consistent with the discussion above that compares the  $M_C$  between old globular clusters and young open clusters in low-metallicity environments, but seems to contradict the comparison of  $M_C$  between local star-forming clusters and those in a low-metallicity environment. However, since the lower end of the mass ranges in the Gaia studies do not reach as low as in our study, and the IMF estimated from the Gaia data does not fully cover the IMF peak, we cannot necessarily compare them on the same basis.

Theoretically, the temperature of star-forming clouds drops sharply to a minimum due to the thermal coupling of gas and dust, when fragmentation tends to occur (Larson 2005; Inutsuka & Miyama 1997), and the Jeans mass in these conditions is expected to correspond to the peak value of the IMF. At lower metallicities, higher temperatures and hence higher densities are expected. For the Jeans mass,  $M_J \propto \rho^{-1/2} T^{3/2}$ , the effect of higher density is greater than

that of higher temperature, resulting in lower  $M_J$ . Although this effect has not been explicitly mentioned under the metallicity of  $\sim -1$  dex, the plot of fragmentation masses as a function of heavy elements (Omukai et al. 2005) seems to indicate a trend toward smaller fragmentation masses corresponding to lower temperature minima with decreasing metallicity. Recent simulation studies (e.g., Bate 2019, Chon et al. 2021) also indicate that the peak mass gradually decreases from  $Z/Z_\odot = 10^{-1}$ , which is consistent with the results here, but the difference in  $M_C$  values from those at solar metallicity is seen in  $Z/Z_\odot \lesssim 10^{-4}$ , which is much smaller than the metallicity discussed here. The derivation of  $M_C$  with high accuracy from observations will help constrain theoretical studies and improve understanding of star formation in the future.

For star-forming clusters located in the range of  $R_G \sim 6\text{--}12$  kpc, Damian et al. (2021) derived  $M_C$  to study the possible impact of environmental factors on the form of the IMF at the low-mass end, using photometry from UKIDSS (United Kingdom Infrared Deep Sky Survey) and Gaia parallaxes. They conclude that there is no strong evidence for an environmental effect in the underlying form of the IMF of their target clusters. This seems to contradict the results here, but it may be due to the fact that our results also have large uncertainties, and that their targets may not have large metallicity differences, or perhaps the spatial resolution (FWHM = 0.8–1.0 arcsec) and sensitivity ( $K \lesssim 18$  mag) of UKIDSS may not be sufficient to resolve low-mass stars.

The IMFs of young star-forming clusters in low-metallicity environments have been studied for the outer Galaxy (see Section 1). Among them, a recent work (Yasui et al. 2023), which is the basis for the KLF fit in this paper, has for the first time derived detailed IMFs down to  $\simeq 0.1 M_\odot$  in a low-metallicity environment. While the mass detection limit was found not to cover the second break mass of the IMF, the first break masses were estimated to be  $\simeq 0.1 M_\odot$  for two clusters, which is the upper limit for  $M_C$ . This result is consistent with the  $M_C$  derived here for the Cloud 2 clusters, and may support the suggestion here that low  $M_C$  values are characteristics of low-metallicity environments at least in the Galaxy. The Large and Small Magellanic Clouds (LMC/SMC) would be a more typical target for IMF studies in low-metallicity environments (e.g., Sirianni et al. 2000). However, because mass detection limits had been unable to reach below  $\sim 1 M_\odot$  until very recently, and even JWST can only reach down to  $\sim 0.1 M_\odot$  (Leschinski & Alves 2020) due to the relatively large distance ( $D \simeq 50$  kpc), it is difficult to make direct comparisons of  $M_C$  at this time.

## 6. CONCLUSION

We have presented NIR observations (from 1 to 2  $\mu\text{m}$ ) using JWST/NIRCam for Digel Cloud 2, which is a star-forming region in the Outer Galaxy. Previous studies found two young open clusters located in the northern and southern dense cores of the molecular cloud, the Cloud 2-N and -S clusters, respectively. The metallicity of Cloud 2 was estimated as  $-0.7$  dex. We derived the substellar mass function for the clusters in this low-metallicity environment primarily using NIR NIRCam images in the short wavelength channel (F115W, F150W, and F200W). The main results can be summarized as follows:

1. The distance of the Cloud 2 clusters is estimated to be 7.9 kpc based on recent results from Gaia DR3. Using this distance, the ages of the clusters are estimated as  $\simeq 0.1$  Myr from the projected angular difference of the cluster from the current SNR shell front.
2. The FWHM of 0.07 arcsec is achieved for the F200W band images, leading to a spatial resolution of 550 au. The  $10\sigma$  detection limits, based on pixel-to-pixel noise, reach up to  $m_{\text{F115W}} \simeq 24.5$  mag,  $m_{\text{F150W}} \simeq 24.2$  mag, and  $m_{\text{F200W}} \simeq 23.8$  mag.
3. The spatial extent of the two clusters are identified from the spatial distribution of stellar overdensities detected in the MIRI images, which are very sensitive to star formation activity. The regions have radii of  $\simeq 15$  arcsec. Using the  $(m_{\text{F150W}} - m_{\text{F200W}})$  vs.  $(m_{\text{F115W}} - m_{\text{F150W}})$  color-color diagram for the detected sources, we derived the distributions of reddening, extinction ( $A_V$ ), and F200W-band disk excess (F200W excess). Based on the resulting distribution of  $A_V$ , mass- $A_V$ -limited samples whose low-mass limit is estimated as  $\simeq 0.02 M_\odot$  for both Cloud 2-N and -S clusters are extracted using the color-magnitude diagram. Using the mass- $A_V$ -limited samples, cluster F200W-band luminosity functions (F200W-LFs) are derived with the mass detection limits of  $\simeq 0.02 M_\odot$  for both clusters.
4. Based on the fitting of F200W-LFs by assuming log-normal and TPL IMFs, the best derived IMFs are found to cover the characteristic mass of  $\log M_C/M_\odot \simeq -1.5$  ( $0.03 M_\odot$ ). This is the first derivation of  $M_C$  for young

open clusters in a low-metallicity environment and was achieved due to the high sensitivity of JWST. Furthermore, the detection of low-mass sources in the mass range of brown dwarfs ( $\lesssim 0.08 M_{\odot}$ ) in a low-metallicity cluster is an important aspect of this observation because brown dwarfs cannot sustain hydrogen fusion and are not found in old clusters.

5. Very similar values of  $M_C$  are obtained for the Cloud 2-N and -S clusters, suggesting that these values are typical for this region. It should be noted, however, that the  $M_C$  values obtained here are subject to various uncertainties in addition to the uncertainty from the F200W-LF fitting.
6. The derived  $M_C$  values for the Cloud 2 clusters are generally lower than previous derivations for nearby regions. In particular, the lower  $M_C$  compared to local star-forming open clusters, which have similar ages ( $\sim 10^6$ – $10^7$  yr) and cluster scales ( $N_* \lesssim 10^3$ ), suggests a metallicity dependence of  $M_C$ . The lower  $M_C$  compared to local globular clusters, which are old systems ( $\sim 10^{10}$  yr), suggests that the Cloud 2 clusters are very young and have not yet undergone dynamical evolution, where the present-day mass function literally reflects the initial mass function. Although there appears to be no explicit theoretical mention of  $M_C$  below metallicities of  $\sim -1$  dex, deriving  $M_C$  values with high accuracy from observations in such environments would place significant constraints on future theoretical studies and improve our understanding of star formation.

We thank the anonymous referee for useful comments and suggestions that helped to improve the manuscript. We also thank Kazuyuki Omukai and Sunmyon Chon for useful discussions on theoretical aspects of the IMF in low-metal environments, and Yuji Ikeda for helpful discussion on statistics. C.Y. is supported by KAKENHI (18H05441) Grant-in-Aid for Scientific Research on Innovative Areas. The model fitting was performed using the Multi-wavelength Data Analysis System operated by the Astronomical Data Center (ADC) of the National Astronomical Observatory of Japan. The work of MER was carried out at the Jet Propulsion Laboratory, California Institute of Technology, under a contract with the National Aeronautics and Space Administration (80NM0018D0004). The data presented in this article were obtained from the Mikulski Archive for Space Telescopes (MAST) at the Space Telescope Science Institute. The specific observations analyzed can be accessed via [DOI](#).

*Facilities:* JWST (NIRCam and MIRI), Subaru

*Software:* IRAF (Tody 1986, 1993), synphot (STScI Development Team 2018), JWST Calibration Pipeline Version (Bushouse et al. 2023)

**Table 1.** The  $10\sigma$  detection limits for JWST/NIRCam Observations

Region	F115W (mag)	F150W (mag)	F200W (mag)
Cloud 2-N	24.6	24.2	23.6
Cloud 2-S	24.8	24.6	23.8
Control	24.6	24.6	23.8

**Table 2.** The best-fit parameters of the Log-normal IMF ( $dN/d\log m \propto \exp(-C \times (\log m - \log M_C))$ ) for the Cloud 2-N and -S clusters

Cluster	$C$	$\log M_C$
Cloud 2-N	1.1 [0.1, 4.2]	-1.5 [-1.7, -1.4]
Cloud 2-S	3.1 [0.9, 6.9]	-1.6 [-2.0, -1.4]

Note. The range of the 68% confidence level are shown in parentheses.

**Table 3.** The best-fit parameters of the TPL IMF ( $dN/d\log m \propto m^{-\Gamma} \{1 - \exp[-(m/M_C)^\beta]\}$ ) for the Cloud 2-S cluster

Cluster	$\Gamma$	$\log M_C$	$\beta$
Cloud 2-S	0.9 [0.7, 2.0]	-1.4 [-1.7, -1.0]	1.9 [0.9, 4.0]

Note. The range of the 68% confidence level are shown in parentheses.

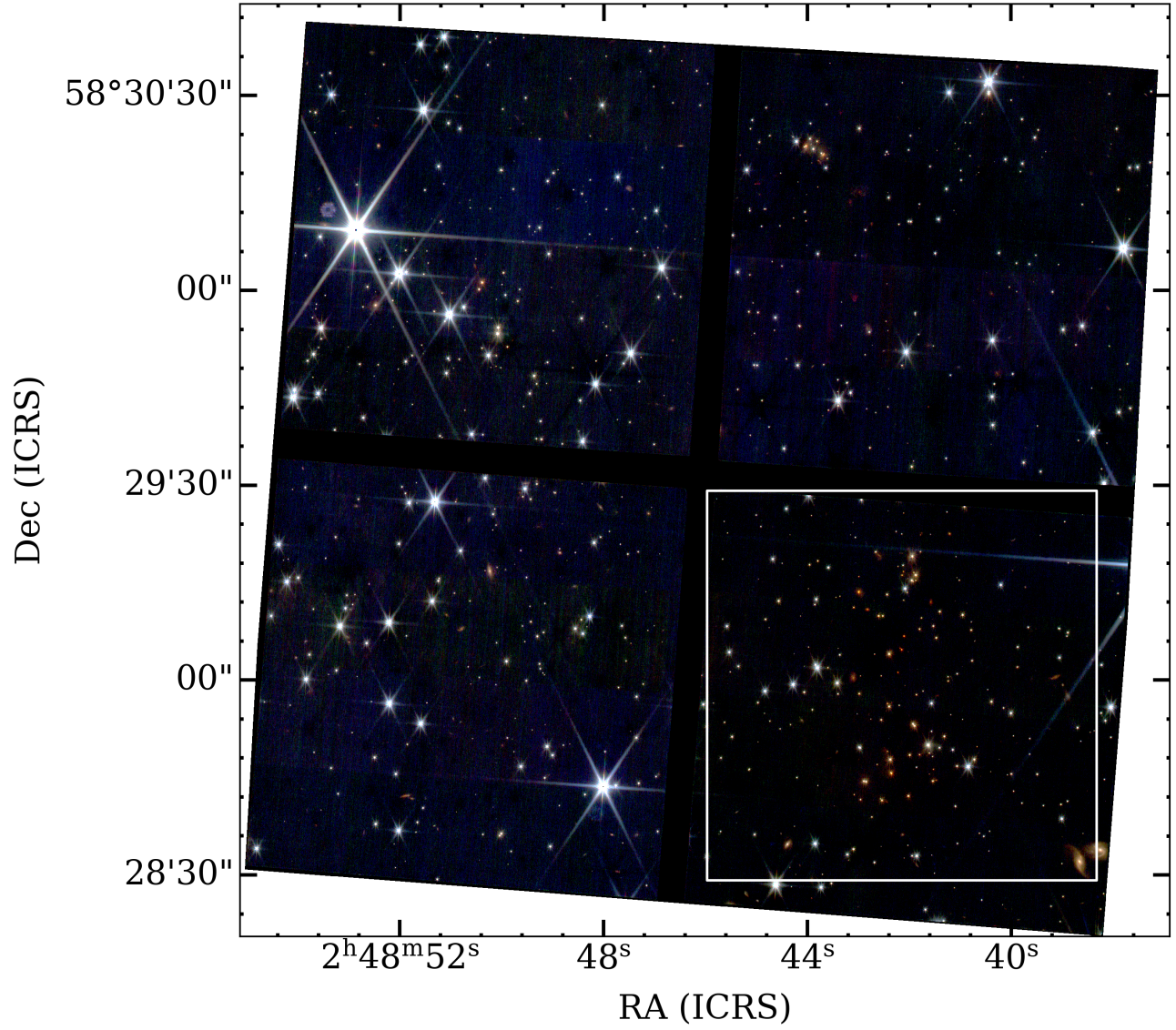


**Figure 1.** Pseudocolor images of Cloud 2-N obtained with JWST/NIRCam produced by combining the NIR images, F115W (blue), F150W (green), and F200W (red). The solid white square indicates the 1 arcmin square centered on the Cloud 2-N cluster, shown in Figure 3.



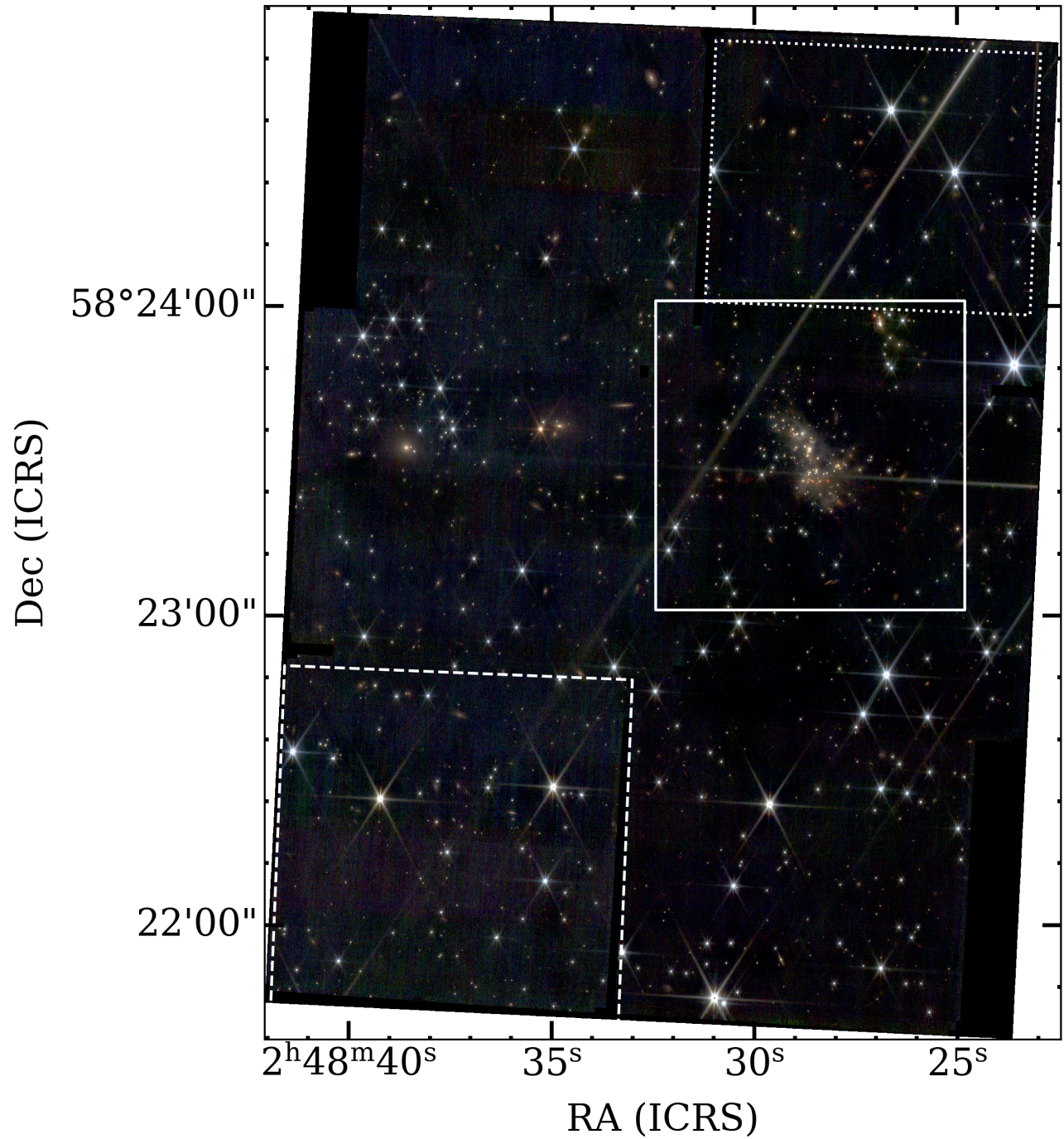


**Figure 2.** Pseudocolor images of Cloud 2-S obtained with JWST/NIRCam produced by combining the NIR images, F115W (blue), F150W (green), and F200W (red). The solid white square indicates the 1 arcmin square centered on the Cloud 2-S cluster, shown in Figure 3, while the white dashed square shows the control field. An additional control field is indicated by a dotted square.

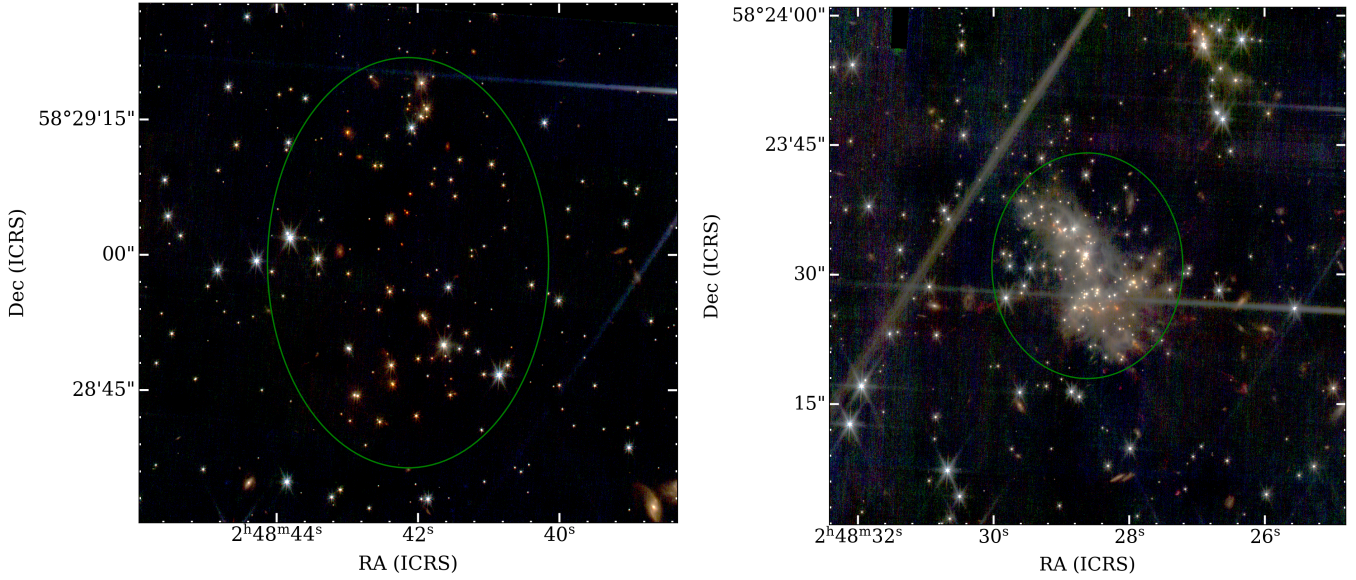


**Figure 3.** Zoomed in F200W-band images of the Cloud 2-N and -S clusters. North is up and east is left. The areas of the images are indicated by the white squares in figures 1 and 2, with the field of view of about  $1' \times 1'$ . The positions of the cluster regions, which are identified in Section 3.1 from the regions where particularly high stellar densities were detected in the MIRI images (Izumi et al. 2024), are shown as green ellipses.

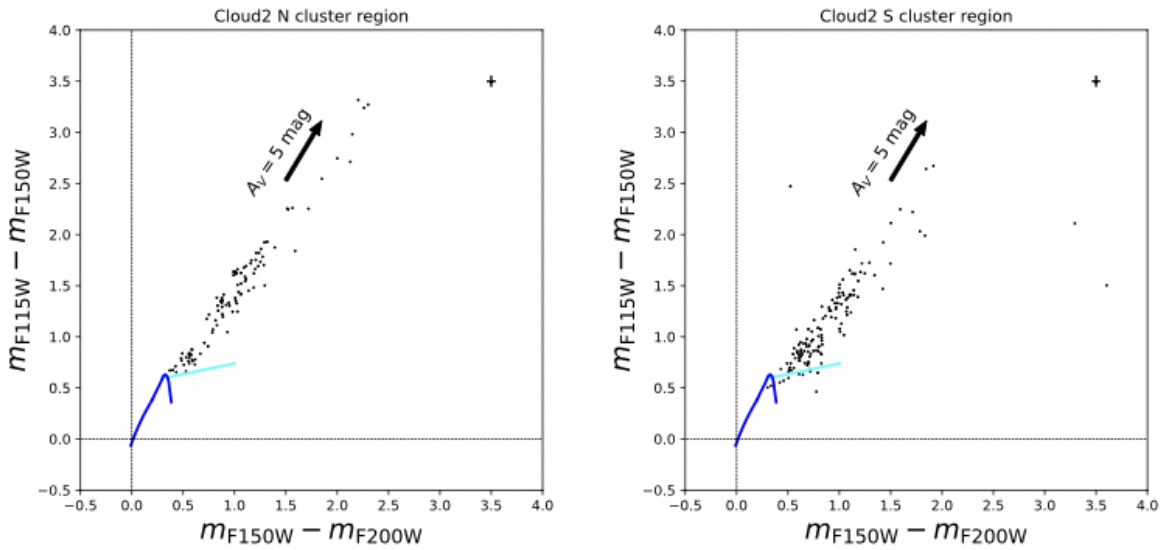


**Figure 4.**  $(m_{F150W} - m_{F200W})$  vs.  $(m_{F115W} - m_{F150W})$  color-color diagrams for the Cloud 2-N cluster region (*left*) and the 2-S region (*right*). The blue curve in the lower left portion of each diagram is the locus of points corresponding to unreddened main-sequence stars. The loci of classical T Tauri star (CTTS) are shown with cyan lines. The black arrows show the reddening vectors for  $A_V = 5$  mag. Typical uncertainty ( $1\sigma$ ) of the colors are shown at the top-right corner.

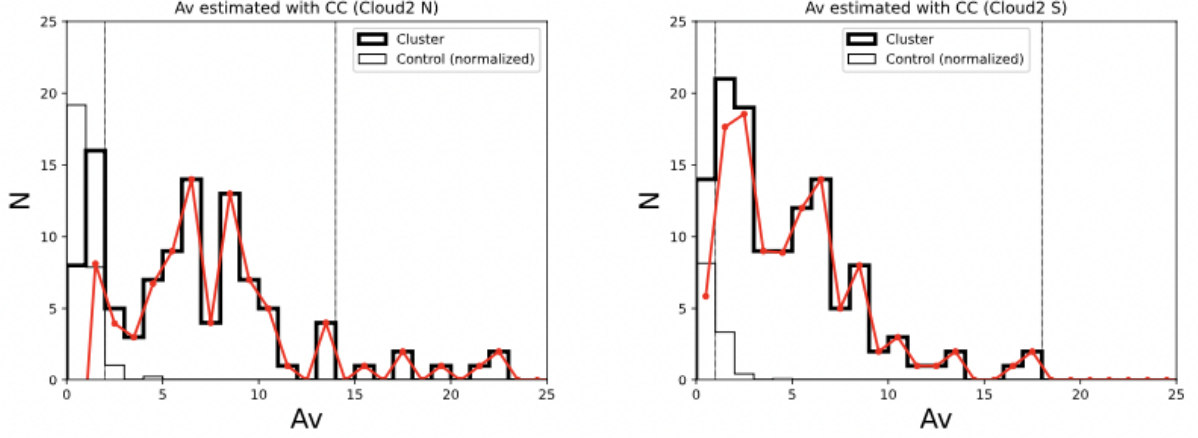


**Figure 5.**  $A_V$  distributions for stars in the regions of the Cloud 2-N cluster (left panel) and of the 2-S cluster (right panel). The distributions for stars in the cluster regions are shown as thick lines, while those in the control field are shown as thin lines. The distributions for stars in the control field are normalized by multiplying the ratio of the area of each cluster region to the area of the control field. The distributions obtained by subtracting the normalized distribution for stars in the control field from the distribution for stars in the cluster regions are shown as red lines. The vertical dotted lines show the  $A_V$  ranges of the Cloud 2 clusters set in Section 3.3 for defining the mass- $A_V$ -limited sample.

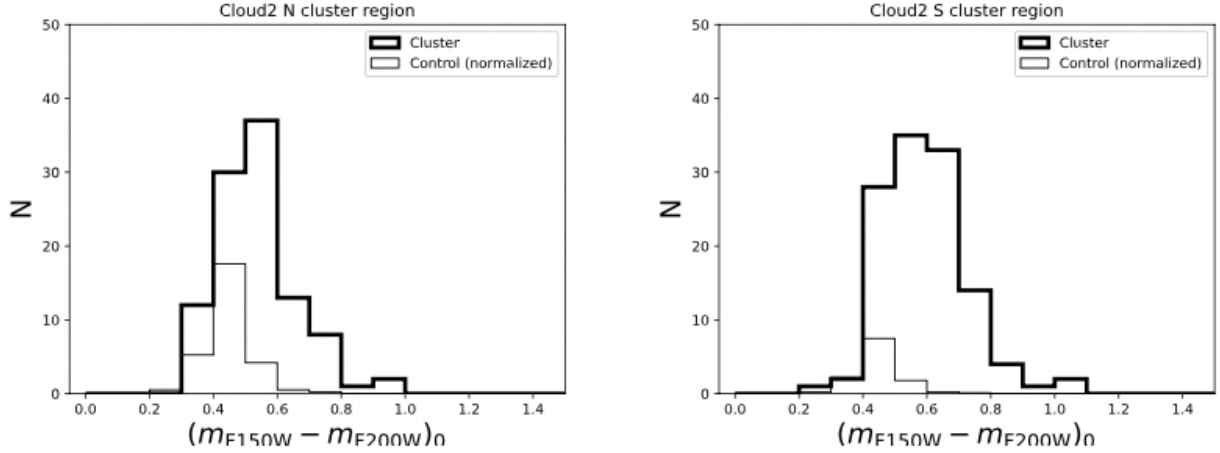


**Figure 6.** Distributions of  $(m_{F115W} - m_{F150W})_0$  for stars in the regions of the Cloud 2-N cluster (left panel) and of the Cloud 2-S cluster (right panel). The distributions for stars in the cluster regions are shown as thick lines, while those in the control field are shown as thin lines. The distributions for stars in the control field are normalized by multiplying the ratio of the area of each cluster region to the area of the control field.

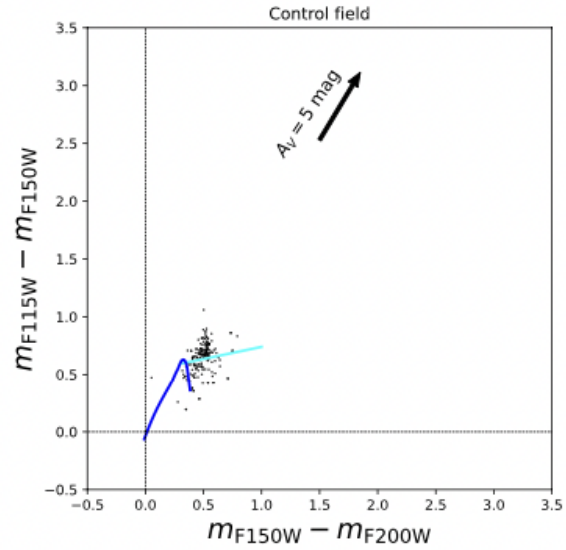


Figure 7. Same figure as Figure 4, but for the control field.

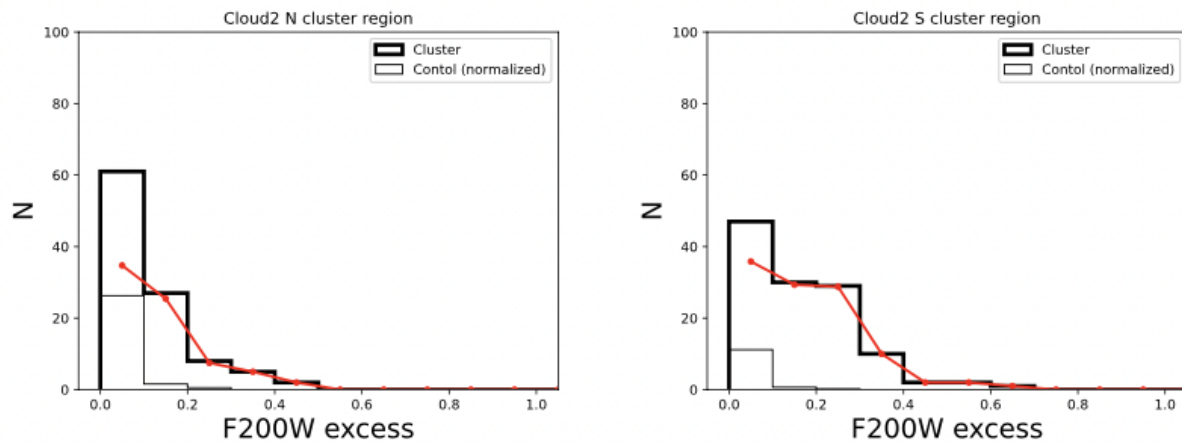
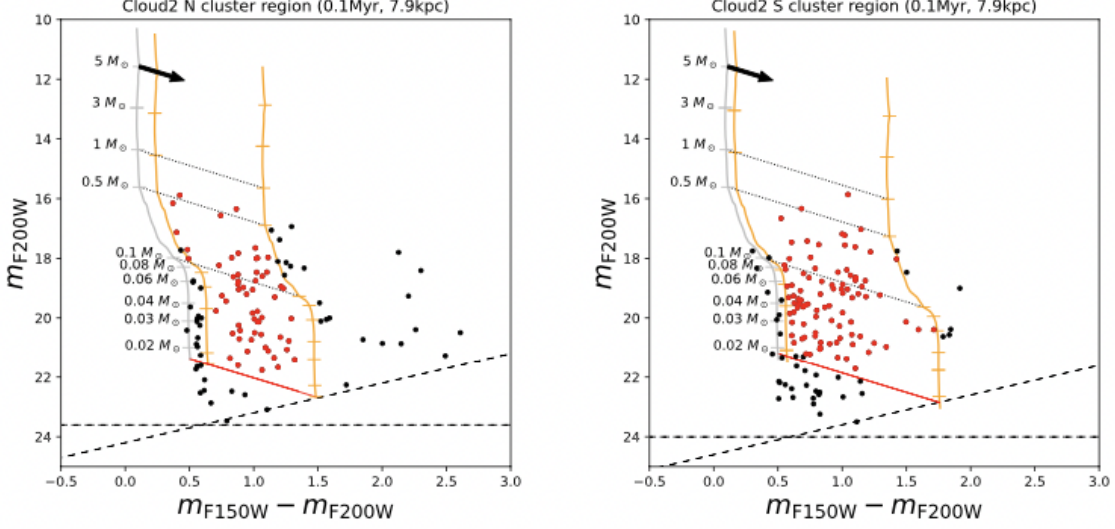
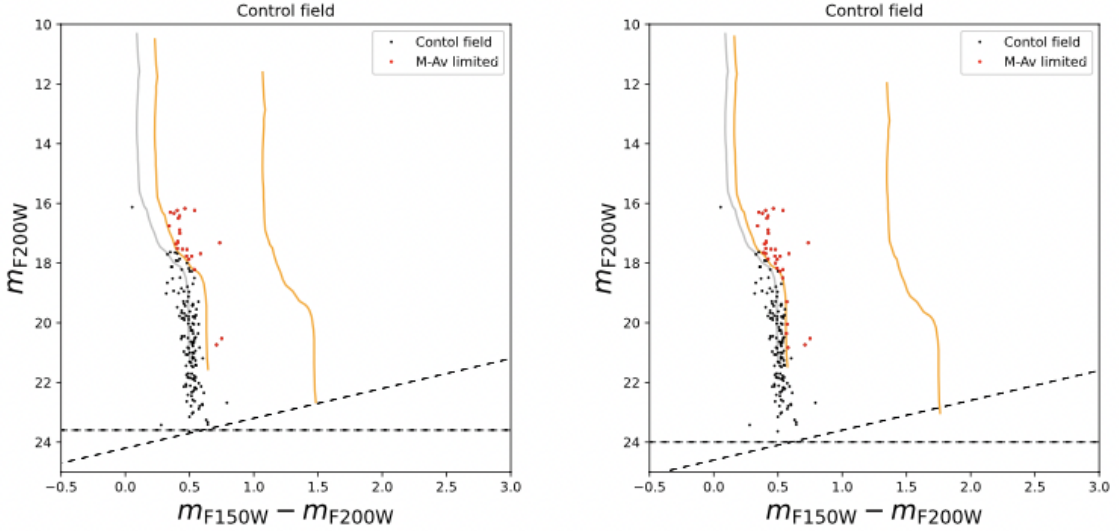


Figure 8. F200W-excess distributions for stars in the regions of the Cloud 2-N cluster (left panel) and of the 2-S cluster (right panel). The distributions for stars in the cluster regions are shown as thick lines, while those in the control field are shown as thin lines. The distributions for stars in the control field are normalized by multiplying the ratio of the area of each cluster region to the area of the control field. The distributions obtained by subtracting the normalized distribution for stars in the control field from the distribution for stars in each cluster region are shown as red lines.



**Figure 9.** ( $m_{F150W} - m_{F200W}$ ) vs.  $m_{F200W}$  color-magnitude diagram for the Cloud 2 clusters. Only point sources located in the cluster region and are detected with more than  $10\sigma$  in both the F150W and F200W bands are plotted. The gray lines show isochrone models from Siess et al. (2000) for the mass range  $3 < M/M_{\odot} \leq 7$ ; and from D’Antona & Mazzitelli (1997) for the mass range  $0.017 \leq M/M_{\odot} \leq 3$ . A distance of 7.9 kpc and the age of 0.1 Myr are assumed. The black arrows show the reddening vectors for  $A_V = 5$  mag from the isochrone models. Stars located in the cluster region on the sky and are located between the orange lines on the color-magnitude diagram ( $2 \leq A_V \leq 14$  mag and  $1 \leq A_V \leq 18$  mag for the Cloud 2-N and -S clusters, respectively), are identified as cluster members. Identified cluster members are shown as red dots, while sources that are located in the cluster region but which are not considered to be cluster members shown as black dots. The dashed lines show the  $10\sigma$  limits. The sensitivity limits are indicated by red lines.



**Figure 10.** Same figure as Figure 9, but for the control field. The left and right panels are for the same control field, but just apply different  $A_V$  thresholds for each cluster, the left and right panels ( $2 \leq A_V \leq 14$  mag and  $1 \leq A_V \leq 18$  mag) for the Cloud 2-N and -S clusters, respectively.

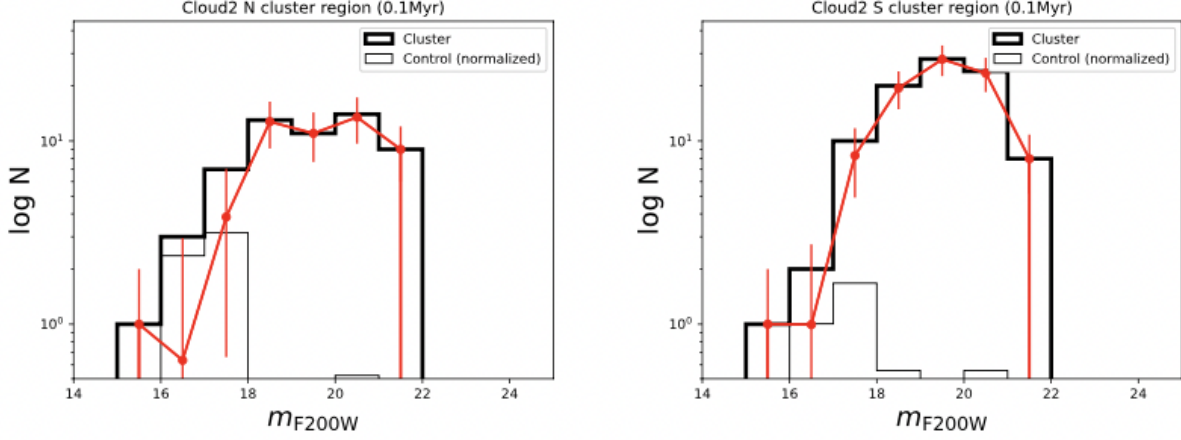


**Figure 11.** The observed F200W-LFs for the Cloud 2 clusters (Cloud 2-N and -S clusters for the left and right panels, respectively). The F200W-LFs for sources in the cluster regions (the cluster region F200W-LFs) are shown with thick black lines, while those for sources in the control field (the control field F200W-LF) are shown with thin lines. The control field F200W-LF is normalized by multiplying the ratio of the area of each cluster region to the area of the control field. The cluster F200W-LFs, obtained by subtracting the normalized counts from the control field F200W-LF from the counts for each cluster region F200W-LF, are shown as thick red lines.

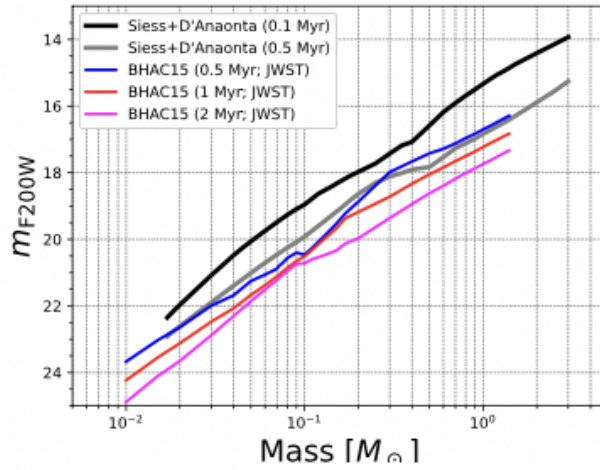


**Figure 12.** Comparison of theoretical mass-luminosity ( $m_{F200W}$ ) relations. The M–L relation that is used in the modeling in Section 4.1 (Siess et al. 2000; D’Antona & Mazzitelli 1997, 1998) for the age of 0.1 Myr is shown with a black line, while the relation by the same reference but for the age of 0.5 Myr is shown with a gray line. The M–L relations in the JWST/NIRCam filter system by Baraffe et al. (2015) for the ages of 0.5, 1, and 2 Myr are shown with blue, red, and magenta lines, respectively. The distance of  $D = 7.9$  kpc is assumed.

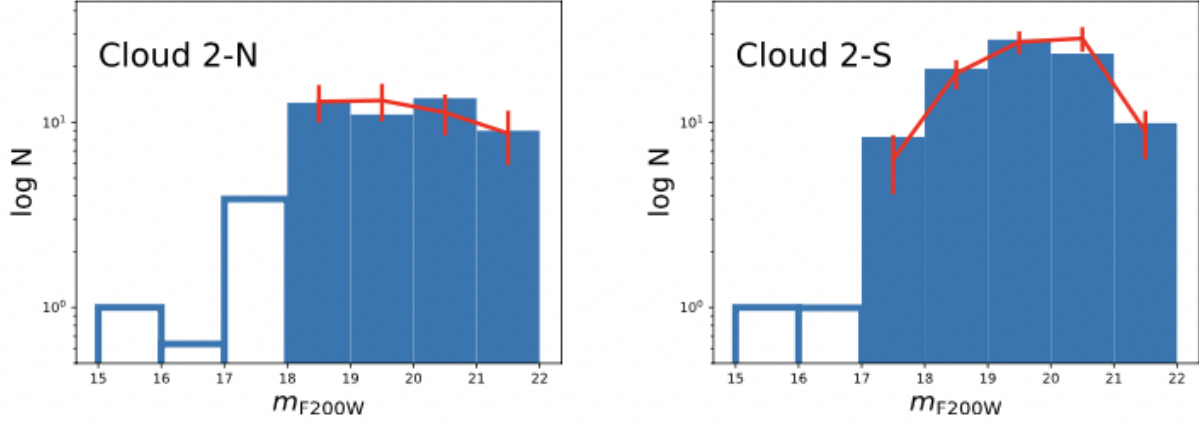


**Figure 13.** Model F200W-LF with the parameters of the best-fit IMF for the Cloud 2-N and -S clusters. The best-fit model F200W-LF is shown as the red line with  $1\sigma$  standard deviation, which are from 100 trials for the best-fit log-normal/TPL IMF parameter sets for the Cloud 2-N/-S clusters, while the observed cluster KLF for the age is shown as the blue histogram. The bins of the fit range are indicated by filled blue squares, and the others by open blue squares.

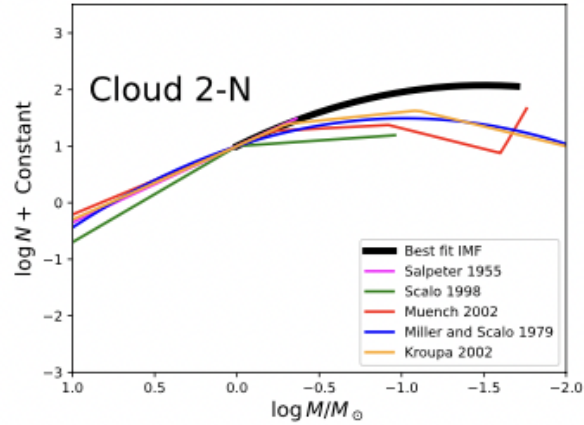


**Figure 14.** The best-fit IMF for the Cloud 2-N cluster. The best-fit IMF assuming a log-normal IMF is shown as the black line. The cluster IMF is also compared to IMFs previously obtained in the field and in nearby star clusters: Salpeter (1955, magenta), Scalo (1998, green), Muench et al. (2002, red), Miller & Scalo (1979, blue), and Kroupa (2002, orange). All of the IMFs are normalized to 0 on the vertical axis at a mass of  $1 M_{\odot}$ .

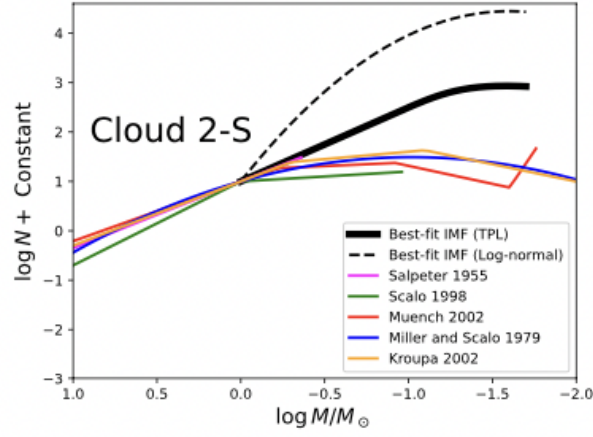


**Figure 15.** The best-fit IMF for the Cloud 2-S cluster. The best-fit IMFs assuming the TPL/log-normal IMFs are shown as the black thick/dashed lines. The cluster IMF is also compared to IMFs previously obtained in the field and in nearby star clusters: Salpeter (1955, magenta), Scalzo (1998, green), Muench et al. (2002, red), Miller & Scalzo (1979, blue), and Kroupa (2002, orange). All of the IMFs are normalized to 0 on the vertical axis at a mass of  $1 M_{\odot}$ .



## APPENDIX

## A. COLOR TRANSFORMATIONS BETWEEN THE NIRCAM PHOTOMETRIC SYSTEM AND THE MKO SYSTEM

Synthetic photometry was generated for the JWST/NIRCam photometric system, based on Hewett et al. (2006), who generated synthetic photometry for the MKO and other filter systems. The spectra for 151 sources from the Bruzual-Persson-Gunn-Stryker Atlas (Gunn & Stryker 1983) are used as in Hewett et al. (2006). The atlas includes dwarfs (spectral type B9V–M6V), giants (A3III–M7III), and stars of other luminosity classes (including those of unknown spectral types). All magnitude and color calculations are performed using the Python synphot package (STScI Development Team 2018). JWST+NIRCam throughput curves (version 5.0: November 2022) were used. The magnitudes are based on the Vega system by using a reference spectrum for Vega from Bohlin et al. (2020). In addition to the NIRCam filter system, synthetic photometry for the MKO filter system was generated, according to Hewett et al. (2006).

Differences between JWST/NIRCam F115W, F150W, and F200W band magnitudes and MKO-system J, H, and K magnitudes, as a function of MKO colors are shown in the leftmost panels and third panels from the left in Figure 16. Dwarfs and giants are shown with black filled circles and gray filled squares, while the other stars are shown with open circles. As pointed out for the color transformations between the MKO and 2MASS systems in Leggett et al. (2006), the same intrinsic dependencies on luminosity class (between red giants and dwarfs) in red stars are also seen in the figures. The range where the color-to-magnitude conversion is uniquely determined and where the color conversion seems feasible is enclosed by a dashed line, and an enlarged view is shown to the right of each panel. Among these, those with relatively large color ranges (more than 0.4) are indicated by thick dashed lines, and the color transformations are derived by linear fitting as follows:

$$m_{\text{F115W}} - J_{\text{MKO}} = (0.204 \pm 0.010) \times (J - K)_{\text{MKO}} + (0.006 \pm 0.005) \text{ for } (J - K)_{\text{MKO}} \leq 0.9 \quad (\text{A1})$$

$$m_{\text{F115W}} - J_{\text{MKO}} = (0.257 \pm 0.014) \times (J - H)_{\text{MKO}} + (0.005 \pm 0.006) \text{ for } (J - H)_{\text{MKO}} \leq 0.7 \quad (\text{A2})$$

$$m_{\text{F150W}} - H_{\text{MKO}} = (0.291 \pm 0.003) \times (J - H)_{\text{MKO}} + (0.004 \pm 0.001) \text{ for } (J - H)_{\text{MKO}} \leq 0.45 \quad (\text{A3})$$

$$m_{\text{F200W}} - K_{\text{MKO}} = (0.014 \pm 0.002) \times (J - K)_{\text{MKO}} + (0.005 \pm 0.001) \text{ for } (J - K)_{\text{MKO}} \leq 0.65 \quad (\text{A4})$$

In Section 2.3, the objects in the observation field of view that were also detected with Subaru/MOIRCS and have colors in the range where color transformations can be obtained were selected. The sources are used as standard stars by obtaining their NIRCam magnitudes using the color transformations from the MKO to the NIRCam systems.

## B. COLOR-COLOR DIAGRAM IN THE NIRCAM PHOTOMETRIC SYSTEM

The CTTS locus was originally derived in the CIT (California Institute of Technology) system (gray solid line in Figure 17), and Yasui et al. (2008) derived the locus in the MKO system (gray dashed line in Figure 17) by obtaining CTTS colors from a 2MASS catalog in the 2MASS system and converting them to those in the MKO system using color transformations by Leggett et al. (2006). To derive the CTTS locus in the NIRCam system using the same method, the color transformations between NIRCam and 2MASS are necessary. Using the magnitude differences in the 2MASS and MKO systems presented by Hewett et al. (2006) and those in the NIRCam and MKO systems obtained in Appendix A, we compared the magnitudes in the NIRCam and 2MASS systems and found that it is difficult to fit for  $m_{\text{F200W}} - K$  magnitude differences on the red side ( $(J - K)_{2\text{MASS}} \gtrsim 0.7$  mag or  $(H - K)_{2\text{MASS}} \gtrsim 0.1$  mag), as in the case of magnitude differences in the NIRCam and MKO systems. Because CTTSs have actual red colors (intrinsic colors  $(J - H)_0 \simeq 0.5\text{--}1.0$  mag or  $(H - K)_0 \simeq 0.2\text{--}1.0$  mag), it is difficult to obtain colors in the NIRCam system by converting from the color in the 2MASS system.

Instead, we examined the color differences in the NIRCam and MKO systems to determine the differences in the CTTS locus between the systems, using the synthetic photometry obtained in Appendix A. Figure 18 shows magnitude comparison between NIRCam  $m_{\text{F115W}} - m_{\text{F150W}}$  and MKO  $J - H$  in the left panel, and NIRCam  $m_{\text{F150W}} - m_{\text{F200W}}$  and MKO  $H - K$  in the right panel. Because YSOs without disks are known to show dwarf-like colors (see Figure 1 in Meyer et al. 1997 for WTTSs), only dwarfs are shown. For the comparison of NIRCam ( $m_{\text{F115W}} - m_{\text{F150W}}$ ) vs. MKO  $J - H$

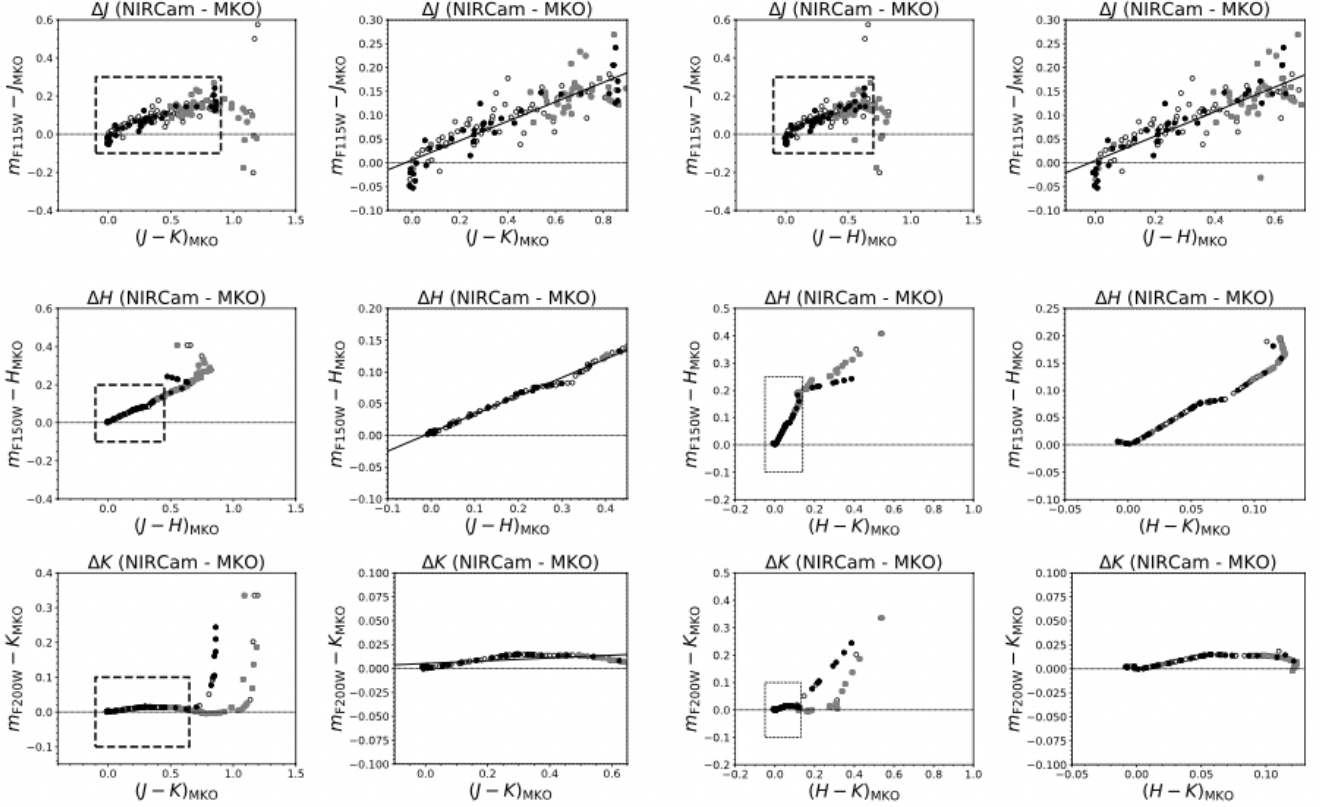


**Figure 16.** Differences between the MKO-system and the JWST/NIRCam-system magnitudes, as functions of the MKO-system colors. In the first and third columns, dwarfs and giants are shown with black filled circles and gray filled squares, while the other stars are shown with open circles. The range where the color-to-magnitude conversion is uniquely determined and where the color conversion seems feasible is enclosed by a dashed line, and an enlarged view is shown to the right of each panel (the second and fourth columns). Among these, those with relatively large color ranges (more than 0.4) are enclosed by thick dashed lines in the first and third columns, and the results of fits are shown with thick lines in second and fourth columns.

on all range plots yields  $(m_{F115W} - m_{F150W}) = (0.969 \pm 0.026) \times (J - H)_{\text{MKO}} + (-0.012 \pm 0.009)$ , shown with a solid line, indicating that the two colors are the same within the uncertainties. For the comparison of NIRCam ( $m_{F150W} - m_{F200W}$ ) vs. MKO  $H - K$  on all range plots yields  $(m_{F150W} - m_{F200W}) = (1.592 \pm 0.048) \times (J - H)_{\text{MKO}} + (0.048 \pm 0.007)$ . However, the comparison between the two colors shows a break at  $H - K \simeq 0.15$ . Fitting the plots up to the break ( $H - K \leq 0.15$ ) yields  $(m_{F150W} - m_{F200W}) = (2.321 \pm 0.035) \times (H - K)_{\text{MKO}} + (-0.008 \pm 0.003)$  (shown as a dot-dash line). The plots after the break ( $H - K \geq 0.15$ ) are distributed over a wide range of horizontal directions, which are located on the left side of the dashed line showing  $m_{F150W} - m_{F200W} = (H - K)_{\text{MKO}}$ . Therefore,  $m_{F150W} - m_{F200W}$  have values between 1 and 2.3 times the MKO  $(H - K)$  colors. In summary, the CTTS locus in the NIRCam is shown with a black line in Figure 17, but it can be located in the hatched area in the figure. The results are used in Sections 3.2 to estimate the reddening for each source and to derive reddening properties for the Cloud 2 clusters.

In addition, in Figure 17, the dwarfs in the JWST/NIRCam filter system from the synthetic photometry are shown as black dots on the  $(m_{F115W} - m_{F200W})$  vs.  $(m_{F115W} - m_{F150W})$  color-color diagram. The dwarf star track is shown with a blue curve, which is derived from eye-fit. For comparison, the dwarf-star track for the Johnson-Glass system (Bessell & Brett 1988) and that for the MKO system (Yasui et al. 2008) in the JHK color-color diagram ( $H-K$  and  $J-H$  for horizontal and vertical axes, respectively) are shown with a gray solid line and gray dashed line, respectively. In addition, the reddening vector ( $A_V = 1$  mag) for the NIRCam system from Wang & Chen (2019) is shown as a black arrow.

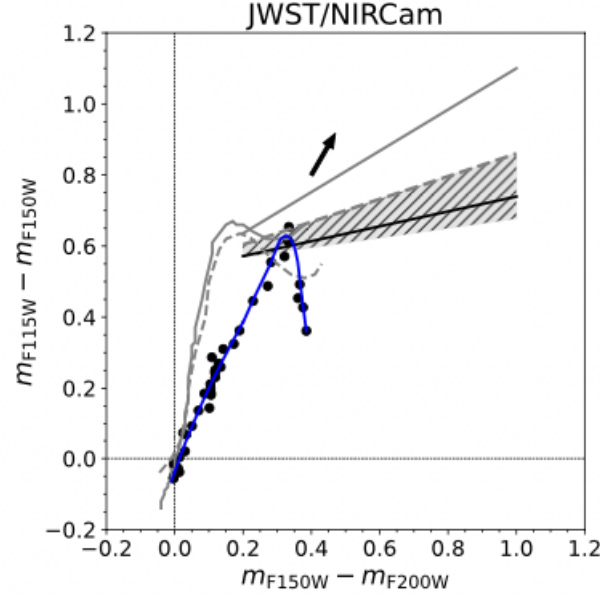


**Figure 17.**  $(m_{F115W} - m_{F200W})$  vs.  $(m_{F115W} - m_{F150W})$  color-color diagram in the JWST/NIRCam filter system. The dwarf stars are shown as black circles, and the dwarf track is shown as a blue curve. For comparison, the track in the Johnson-Glass system (gray solid curve; Bessell & Brett 1988) and that in the MKO system (gray dashed curve; Yasui et al. 2008) are shown. The area where the CTTS locus is located in the NIRCam system is indicated by the hatched area, along with the locus in the CIT system (gray solid line; Meyer et al. 1997) and that in the MKO system (gray dashed line; Yasui et al. 2008). The arrows indicate the reddening vector for  $A_V = 1$  mag from Wang & Chen (2019).

## REFERENCES

- Andersen, M., Meyer, M. R., Greissl, J., et al. 2008, *ApJL*, 683, L183.
- Bailer-Jones, C. A. L., Rybizki, J., Fousneau, M., et al. 2021, *AJ*, 161, 147.
- Baraffe, I., Homeier, D., Allard, F., et al. 2015, *A&A*, 577, A42.
- Bate, M. R. 2019, *MNRAS*, 484, 2341.
- Bessell, M. S., & Brett, J. M. 1988, *PASP*, 100, 1134
- Bohlin, R. C., Hubeny, I., & Rauch, T. 2020, *AJ*, 160, 21.
- Bouvier, J., Grankin, K., Ellerböck, L. E., et al. 2013, *A&A*, 557, A77. doi:10.1051/0004-6361/201321389
- Bushouse, H., Eisenhamer, J., Dencheva, N., et al. 2023, Zenodo
- Chabrier, G. 2003, *ApJL*, 586, L133. doi:10.1086/374879
- Chon, S., Omukai, K., & Schneider, R. 2021, *MNRAS*, 508, 4175.
- Damian, B., Jose, J., Samal, M. R., et al. 2021, *MNRAS*, 504, 2557.
- D’Antona, F., & Mazzitelli, I. 1997, *Memorie della Societa Astronomica Italiana*, 68, 807
- D’Antona, F., & Mazzitelli, I. 1998, *ASP Conf. Ser.* 134: Brown Dwarfs and Extrasolar Planets, 134, 442
- de Geus, E. J., Vogel, S. N., Digel, S. W., et al. 1993, *ApJL*, 413, L97.
- Duchêne, G., Lacour, S., Moraux, E., et al. 2018, *MNRAS*, 478, 1825.
- De Marchi, G., Paresce, F., & Portegies Zwart, S. 2010, *ApJ*, 718, 105.
- Digel, S., de Geus E. J., & Thaddeus, P. 1994, *ApJ*, 422, 92.
- Dieball, A., Bedin, L. R., Knigge, C., et al. 2019, *MNRAS*, 486, 2254.
- Elmegreen, B. G., Klessen, R. S., & Wilson, C. D. 2008, *ApJ*, 681, 365
- Fahrion, K. & De Marchi, G. 2023, *A&A*, 671, L14.
- Gaia Collaboration, Vallenari, A., Brown, A. G. A., et al. 2023, *A&A*, 674, A1.
- Gordon, K. D., Bohlin, R., Sloan, G. C., et al. 2022, *AJ*, 163, 267.
- Gunn, J. E. & Stryker, L. L. 1983, *ApJS*, 52, 121.
- Hallakoun, N. & Maoz, D. 2021, *MNRAS*, 507, 398.

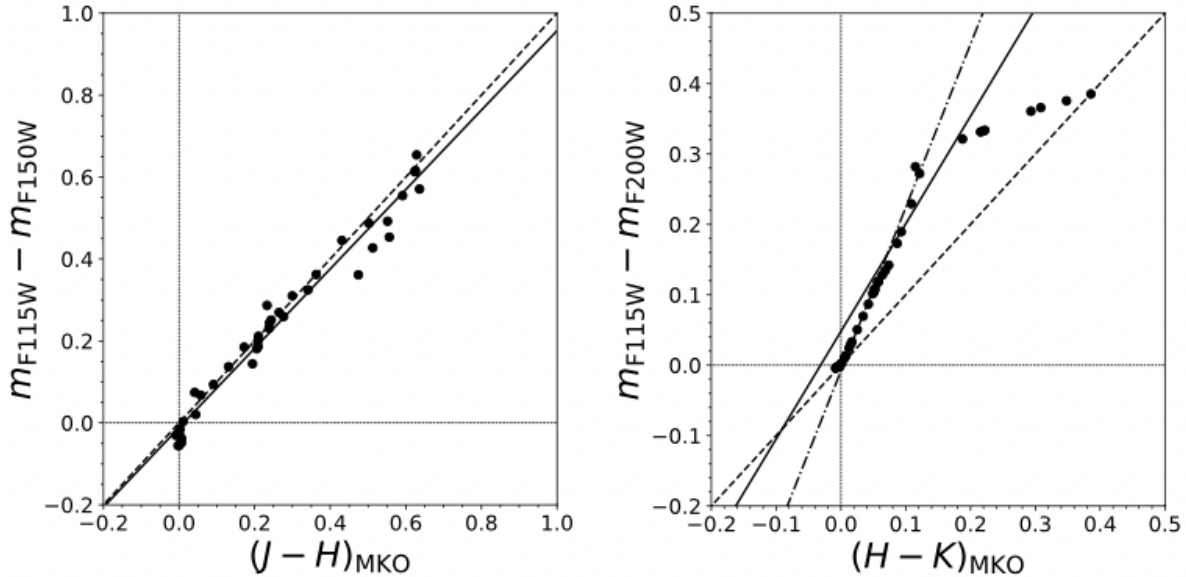


**Figure 18.** Comparison of colors in the NIRCcam and MKO systems. The comparison of NIRCcam ( $m_{F115W} - m_{F150W}$ ) and MKO  $J - H$  are shown in the left panel, while that of ( $m_{F115W} - m_{F200W}$ ) vs. MKO  $H - K$  is shown in the right panel. The dwarfs in the JWST/NIRCcam and MKO filter systems from the synthetic photometry are shown as black dots. The lines show the fits of the plots. (See Appendix B for details of the fits).

Hewett, P. C., Warren, S. J., Leggett, S. K., & Hodgkin, S. T. 2006, *MNRAS*, 367, 454  
 Hillenbrand, L. A. 1997, *AJ*, 113, 1733.  
 Inutsuka, S.-. ichiro . & Miyama, S. M. 1997, *ApJ*, 480, 681.  
 Izumi, N., Kobayashi, N., Yasui, C., et al. 2017, *AJ*, 154, 163.  
 Izumi, N., Ressler, M. E., Lau, R. M., et al. 2024, *AJ*, 168, 68.  
 Kobayashi, N., & Tokunaga, A. T. 2000, *ApJ*, 532, 423  
 Kobayashi, N., Yasui, C., Tokunaga, A. T., & Saito, M. 2008, *ApJ*, 683, 178  
 Kraus, A. L., Ireland, M. J., Martinache, F., et al. 2011, *ApJ*, 731, 8.  
 Kroupa, P. 2002, *Science* 295, 82  
 Lada, C. J., & Adams, F. C. 1992, *ApJ*, 393, 278  
 Lada, C. J., & Lada, E. A. 2003, *ARA&A*, 41, 57  
 Larson, R. B. 2005, *MNRAS*, 359, 211.  
 Leggett, S. K., Currie, M. J., Varricatt, W. P., et al. 2006, *MNRAS*, 373, 781.  
 Leschinski, K. & Alves, J. 2020, *A&A*, 639, A120.  
 Li, J., Liu, C., Zhang, Z.-Y., et al. 2023, *Nature*, 613, 460.  
 Lubowich, D. A., Brammer, G., Roberts, H., Millar, T. J., Henkel, C., & Pasachoff, J. M. 2004, in *Origin and Evolution of the Elements*, ed. A. McWilliam, & M. Rauch (Carnegie Observ. 4; Cambridge: Cambridge Univ. Press), 37

Luhman, K. L., Rieke, G. H., Young, E. T., et al. 2000, *ApJ*, 540, 1016.  
 Meyer, M. R., Calvet, N., & Hillenbrand, L. A. 1997, *AJ*, 114, 288  
 Miller, G. E., & Scalo, J. M. 1979, *ApJS* 41, 513  
 Minowa, Y., Kobayashi, N., Yoshii, Y., et al. 2005, *ApJ*, 629, 29.  
 Moe, M., Kratter, K. M., & Badenes, C. 2019, *ApJ*, 875, 61.  
 Muench, A. A., Lada, E. A., & Lada, C. J. 2000, *ApJ*, 533, 358  
 Muench, A. A., Lada, E. A., Lada, C. J., & Alves, J. 2002, *ApJ*, 573, 366  
 Muench, A. A., Lada, E. A., Lada, C. J., et al. 2003, *AJ*, 125, 2029  
 Muzzio, J. C., & Rydgren, A. E. 1974, *AJ*, 79, 864  
 Nardiello, D., Bedin, L. R., Burgasser, A., et al. 2022, *MNRAS*, 517, 484.  
 Nardiello, D., Griggio, M., & Bedin, L. R. 2023, *MNRAS*, 521, L39.  
 Offner S. S. R., Moe M., Kratter K. M., Sadavoy S. I., Jensen E. L. N., Tobin J. J., 2023, *ASPC*, 534, 275.  
 Omukai, K., Tsuribe, T., Schneider, R., et al. 2005, *ApJ*, 626, 627.  
 Paresce, F. & De Marchi, G. 2000, *ApJ*, 534, 870.

- Portegies Zwart, S. F., McMillan, S. L. W., & Gieles, M. 2010, *ARA&A*, 48, 431.
- Rolleston, W. R. J., Smartt, S. J., Dufton, P. L., & Ryans, R. S. I. 2000, *A&A*, 363, 537
- Ruffle, P. M. E., Millar, T. J., Roberts, H., Lubowich, D. A., Henkel, C., Pasachoff, J. M., & Brammer, G. 2007, *ApJ*, 671, 1766
- Rudolph, A. L., Fich, M., Bell, G. R., et al. 2006, *ApJS*, 162, 346.
- Russeil, D., Adami, C., & Georgelin, Y. M. 2007, *A&A*, 470, 161
- Scalo, J. 1998, in *ASP Conf. Ser. 142, The IMF Revisited: A Case for Variations*, ed. G. Gilmore & D. Howell (San Francisco, CA: ASP), 201
- Salpeter, E. E. 1955, *ApJ*, 121, 161.
- Siess, L., Dufour, E., & Forestini, M. 2000, *A&A*, 358, 593
- Simons, D. A., & Tokunaga, A. 2002, *PASP*, 114, 169
- Sirianni, M., Nota, A., Leitherer, C., De Marchi, G., & Clampin, M. 2000, *ApJ*, 533, 203
- Smartt, S. J., Dufton, P. L., & Rolleston, W. R. J. 1996, *A&A*, 305, 164
- Smartt, S. J., & Rolleston, W. R. J. 1997, *ApJL*, 481, L47
- Stephens, D. C., & Leggett, S. K. 2004, *PASP*, 116, 9
- Stil, J. M., & Irwin, J. A. 2001, *ApJ*, 563, 816.
- Strom, K. M., Strom, S. E., Edwards, S., et al. 1989, *AJ*, 97, 1451.
- STScI Development Team 2018, *synphot: Synthetic photometry using Astropy*, *Astrophysics Source Code Library*, ascl:1811.001
- Tokunaga, A. T., Simons, D. A., & Vacca, W. D. 2002, *PASP*, 114, 180
- Tody, D. 1986, *Proc. SPIE*, 627, 733. doi:10.1117/12.968154
- Tody, D. 1993, *Astronomical Data Analysis Software and Systems II*, 52, 173
- Wall, J. V. & Jenkins, C. R. 2012, *Practical Statistics for Astronomers*, by J. V. Wall, C. R. Jenkins, Cambridge, UK: Cambridge University Press, 2012
- Wang, S. & Chen, X. 2019, *ApJ*, 877, 116. doi:10.3847/1538-4357/ab1c61
- Yasui, C., Kobayashi, N., Tokunaga, A. T., et al. 2006, *ApJ*, 649, 753.
- Yasui, C., Kobayashi, N., Tokunaga, A. T., Terada, H., & Saito, M. 2008, *ApJ*, 675, 443
- Yasui, C., Kobayashi, N., Tokunaga, A. T., Saito, M., & Tokoku, C. 2009, *ApJ*, 705, 54
- Yasui, C., Kobayashi, N., Tokunaga, A. T., Saito, M., & Tokoku, C. 2010, *ApJL*, 723, L113
- Yasui, C., Kobayashi, N., Saito, M., et al. 2016b, *AJ*, 151, 115.
- Yasui, C., Kobayashi, N., Tokunaga, A. T., et al. 2016a, *AJ*, 151, 50.
- Yasui, C., Izumi, N., Saito, M., et al. 2017, *Formation and Evolution of Galaxy Outskirts*, 321, 34.
- Yasui, C., Kobayashi, N., Saito, M., et al. 2021, *AJ*, 161, 139
- Yasui, C., Kobayashi, N., Saito, M., et al. 2023, *ApJ*, 943, 137.